ABSTRACT

Circuit Optimization and Frequency Agility for Cognitive Radar

Sarvin Rezayat, M.S.E.C.E.

Mentor: Charles Baylis II, Ph.D.

Due to the increased demand on the spectrum, radars are under increased pressure to participate in dynamic spectrum allocation. To meet these demands, the next generation radar will be an adaptable cognitive radar. This type of radar will require reconfigurable circuitry. This paper explores real-time circuit optimization for a cognitive radar test bench with two types of reconfigurable matching networks. The first one is a varactor matching network that is very quick but experiences non-linearity. The other is an evanescent-mode resonant cavity tuner that handles high input power but experiences stability and repeatability issues. This thesis describes strategies to mitigate the non-ideal behavior of these networks while performing algorithms for circuit optimization. The implementation of frequency agility with circuit optimization is also demonstrated.

Circuit Optimization and Frequency Agility for Cognitive Radar

by

Sarvin Rezayat, B.S.E.C.E.

A Thesis

Approved by the Department of Electrical and Computer Engineering

_____

Kwang, Y. Lee, Ph.D., Chairperson

Submitted to the Graduate Faculty of
Baylor University in Partial Fulfillment of the
Requirements for the Degree
of

Master of Science in Electrical and Computer Engineering

Approved by the Thesis Committee

_____

Charles P. Baylis II, Ph.D., Chairperson

_____

Robert J. Marks II, Ph.D.

_____

Douglas E. Smith, Ph.D.

Accepted by the Graduate School

May 2018

_____

J. Larry Lyon, Ph.D., Dean

Page bearing signatures is kept on file in the Graduate School.

TABLE OF CONTENTS

LIST OF FIGURES

LIST OF TABLES

ACKNOWLEDGMENTS

I would like to thank my advisor Dr. Baylis for guiding me through this work and for always motivating me. I would also like to thank Dr. Marks for his collaboration and always helpful insight. I would also like to thank my coworkers Zach Hays, Luci Hays, Austin Egbert, Casey Latham, Matthew Fellows, and George Toby for the help they have provided me and for the entertainment they have always supplied. I would like to specifically acknowledge Chris Kappelmann for helping develop the material in Chapter Seven. I would like to acknowledge the Army Research Laboratory for funding this research, and I would like to specifically thank our collaborators there who have helped with the development of this research. Lastly, I would like to thank and acknowledge my family for all their support.

CHAPTER ONE

Introduction

With the increased use of wireless devices, modern radar systems are under stricter spectral requirements than ever. This is exemplified by the National Broadband Plan of 2010, which requires 500 MHz of government occupied space to be released for broadband wireless applications before 2020 [1]. To date, spectrum re-allocation and sharing efforts have focused heavily on bands previously dedicated to radar. This means that future radars will have to perform adequately with a less exclusive spectrum. A proposed solution to this issue is dynamic spectrum allocation, in which spectrum is allocated to devices in real time based on their performance objectives and requirements. The nonlinearities of the radar transmitter power amplifier can be a significant contributor to undesirable spectral spreading and must be minimized to allow successful coexistence with other wireless systems in limited bandwidth. In addition to meeting spectral requirements, it is also vital that the system's power amplifier performs efficiently since the power amplifier is typically the largest consumer of power in a radar transmitter.

A cognitive radar is an envisioned type of radar that adjusts its operating behavior and characteristics in real-time to respond to its environment, and it has the potential to allow radars to successfully operate in the spectrum-sharing paradigm of the future [2-3]. A cognitive radar will be able to perform optimally with different spectrum requirements as well as operating frequency. This will require real-time optimization of the circuitry

and waveform of the radar. This thesis presents optimization methods using two different candidate amplifier matching networks that may be eventually implementable in real time. The two matching networks both present different challenges that must be overcome for successful, fast, and accurate reconfiguration. Chapter Two includes a background of the topics that will covered in the thesis as well as some insight into current state of art in this area. Chapter Three demonstrates an optimization using a varactor tuning network. The work presented in this chapter has been previous been accepted to publication in [4]. Chapter Four shows circuit optimization in the Power Smith Tube using the same varactor network. Chapter Five demonstrates circuit optimization using cavity positions of an evanescent mode resonant cavity tuner. Chapter Six demonstrates reconfigurability by adding frequency agility to the optimization. The information contained in Chapter Six was originally accepted for publication in [5]. Chapter Seven provides a conclusion.

CHAPTER TWO

Background

This chapter will provide background information so that following chapters will be more easily comprehended. It also summarizes the state-of-the-art in the subjects covered in this thesis and briefly describes how the research presented in this thesis represents an advancement. Section 2.1 discusses the concept of a cognitive radar. Section 2.2 discusses the concepts involved in circuit optimization. Section 2.3 discusses impedance tuners.

2.1 Background of Cognitive Radar

A cognitive radar is capable of being adaptable. Based on the systems and environment around it, a cognitive radar will adapt to the requirements placed upon it. A key element of a cognitive radar is the ability to perform intelligent signal processing by interacting with the environment around it. This can be implemented through feedback from transmitter to receiver [2]. Intelligent signal processing can include choosing to change operating frequency and bandwidth. This can be achieved by looking at radio frequency interference (RFI) and designing an algorithm to choose the best operating conditions. In order for radars to coexist with wireless communication devices in the electromagnetic environment, they will have to first detect and mitigate interference from RF sources while simultaneously not causing interference to the systems around them. They will then have to modify the radar's bandwidth to comply with regulations. A

cognitive radar will have to be optimized in real-time and continuously. In this aspect, they are reconfigurable.

Reconfigurability for a radar can be achieved by either optimizing the waveform used by the radar or by optimizing the circuitry. It can also be optimized by combining these two methods. Optimizing the waveform of the radar involves optimizing the ambiguity function which aids in improving the range and Doppler resolution. Waveform optimization for radars is an area that has extensively explored, and the latest in this area will be discussed in the next section. Circuit optimization is a less explored area, and it will be discussed in more detail in section 2.2. The research presented in this thesis focuses on circuit optimization for the potential use in a cognitive radar test bench.

2.1.2 State of the Art in Cognitive Radar

The groundwork theory for an adaptive radar has been previously laid out in literature [6-7]. The foundations of a cognitive radar have also been laid out by Haykin and Guerci [2-3]. The S-band has been discussed as a possible region for sharing the spectrum previously and some initial work has been done exploring protocols [8]. Potential solutions using multi-objective optimization sensing technique have been proposed [9]. Work has also been done exploring the fast adaptivity that a cognitive radar requires [10].

Since waveform optimization is also an integral part of cognitive radar, there is extensive work in this area. Rigling and Patton demonstrate waveform optimization techniques using waveform autocorrelation, cross-correlation, and spectrum constraint [11-13]. Waveform optimization has also been explored with hardware-in-the-loop [14-

17]. Latham implements optimization using the ambiguity function properties and spectral mask [18].

2.2 Background of Circuit Optimization

2.2.1 Discussion of Key Concepts

The largest consumer of energy in the transmitter chain of a radar is the power amplifier [4]. This is why it is important that the power-added efficiency (PAE) of the amplifier is maximized. PAE is a metric for the efficiency of an amplifier that takes into account how much DC power input into an amplifier is converted in to radio frequency (RF) power output. It is defined in Equation 2.1 where $P_{out,RF}$ is RF power output of the device, $P_{in,RF}$ is the RF power input into the device, and P_{DC} is the DC power into the device. Ideally a device would have a 100% efficiency, but this is not normally achievable [19].

$$PAE = \frac{P_{out,RF} - P_{in,RF}}{P_{DC}} \times 100\% \tag{2.1}$$

The other parameter used in the optimization is the Adjacent Channel Power Ratio (ACPR). As the name suggests ACPR is the ratio of the adjacent channel to the main channel. Ideally, we want the ACPR to be as small as possible since that means that there is very little spectral spreading. The cause of the spectral spreading is typically amplifier nonlinearities.

A spectral mask is a regulatory set of lines applied to the transmission of a device that the signal has to fall under. More spectral spreading means that there is a larger chance that the device will not meets spectral mask requirements, and therefore interfere

with other devices. Since a spectral mask is used to regulate power in the adjacent channels, an ACPR limit is similar to a spectral mask since they both measure the spectral spreading of a waveform. In the work presented in this thesis, ACPR is used instead of spectral mask because it is an easier metric to measure. In circuit optimization, PAE is optimized with an ACPR limit. An example of a spectral mask is shown in Figure 2.1.

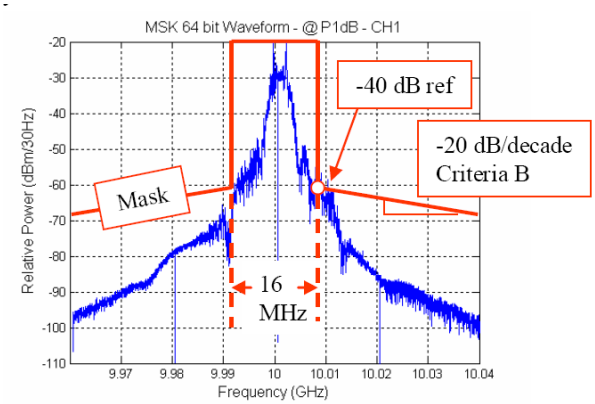

Figure 2.1. Spectral Mask. Reprinted from [20]

The search space for the optimization is the Smith Chart. The Smith Chart is a graphical visualization of reflection coefficient (Γ) that is an extremely helpful tool in amplifier design. Γ is a measure of how much an incident electromagnetic wave is reflected back by an impedance. Both PAE and ACPR are functions of load reflection coefficient (Γ_L). A load-pull measurement can be performed to evaluate and characterize the performance of an amplifier or device over variation in the load reflection coefficient. It is achieved by performing measurements of the criterion (output power, PAE, or ACPR, for example) for changing values of Γ_L around the Smith Chart. Once this data is collected, contours are plotted on the Smith Chart for the measured criteria. Contours are equal-value curves. By plotting these curves for PAE and ACPR, it is possible to view

the values of Γ_L providing maximum PAE and minimum ACPR for a given device and set of device conditions. From an exhaustive load-pull, an estimation of the best PAE that can be obtained while meeting an ACPR constraint can be found. This value will be where the largest PAE contour is located in the ACPR acceptable region. This location is the constrained optimum, and it is where the device acts most efficiently while also assuring spectral compliance. The ACPR acceptable region is the region of the Smith Chart where the ACPR is at or below a pre-specified limit. If the ACPR limit is varied, the collection of the constrained optimum PAE points will form a curve from the PAE optimum to the ACPR minimum and is called the Pareto optimum locus [21]. PAE can be optimized while ACPR is minimized on the Smith Chart by using the real and imaginary parts of Γ_L as an optimization variable. However, PAE and ACPR are also functions of input power and drain voltage. Therefore, this optimization can also be achieved in three dimensions with input power or drain voltage as the third optimization variable. The three-dimensional extension of the Smith Chart is called the Smith Tube. Figure 2.2 shows the Power Smith Tube, which has input power P_{in} as the vertical axis. The Smith Tuneb is an extremely useful visual aid when performing three-dimensional optimization.

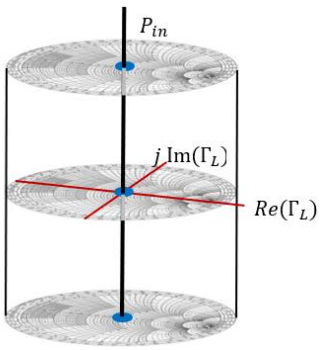

Figure 2.2. The Power Tube. Reprinted from [40]

The optimization technique used for this research is gradient-based convex optimization. Gradient based optimization relies on the idea of climbing in the direction of steepest ascent [22]. The direction of steepest ascent is determined by taking measurements at test or neighboring points which are used in calculating the direction of the gradient. This concept is demonstrated in Figure 2.3 with D_n as the neighboring point distance. At least two points need to be measured in order to estimate the gradient on the Smith Chart. When optimizing in the Smith Tube, three neighboring points are needed since the search space is now three dimensional. However, more neighboring points can be taken for more accuracy. Both ACPR and PAE gradients are calculated but depending on the location of the candidate different steps are taken. Figure 2.4 shows the calculation of the vector to the next candidate point using unit vectors in the direction of PAE steepest ascent ($\hat{p}$) and ACPR steepest descent ($\hat{m}$). If the present candidate is out of spectral compliance, the vector to the next candidate will be chosen as a weighted combination of $\hat{m}$ and the bisector $\hat{b}$, the bisector of $\hat{p}$ and $\hat{m}$ [23]:

$$\bar{v} = \hat{m}D_m + \hat{b}D_b \tag{2.2}$$

If the present candidate is within spectral compliance, the vector to the next candidate will be chosen using a weighted combination of $\hat{p}$ and $\hat{b}$ instead [23]:

$$\bar{v} = \hat{p}D_m + \hat{b}D_b \tag{2.3}$$

The components of the vectors are given by the following [23]:

$$D_m = \frac{D_s}{2}\frac{|ACPR_{meas}|}{|ACPR_{worst}|} \tag{2.4}$$

(2.5)

$$D_b = \frac{D_s}{2} \frac{|\theta_{meas} - \theta_{target}|}{\theta_{target}} \tag{2.6}$$

where $ACPR_{meas}$ is the value of ACPR at the present candidate, $ACPR_{worst}$ is the maximum measured value of ACPR over the entire search, θ_{meas} is the measured value of θ at the candidate, and θ_{target} is 90°, which is the value when the candidate is located on the Pareto optimum locus, where $\hat{p}$ and $\hat{b}$ are oppositely directed. The search stops when the step size to the next candidate falls below a limit set by the user.

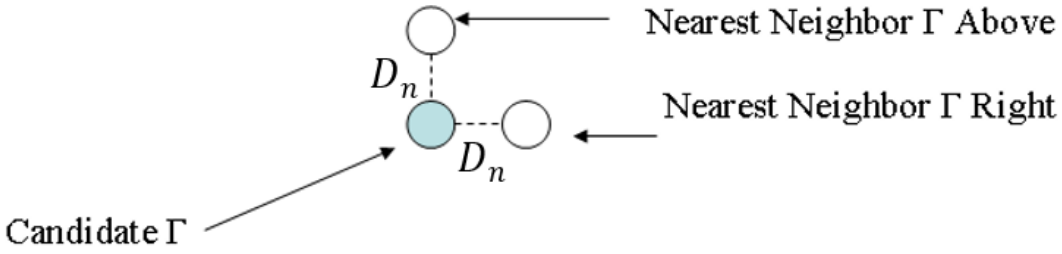

Fig. 2.3. Estimation of the gradient at a candidate value of Γ_L. Reprinted from [23].

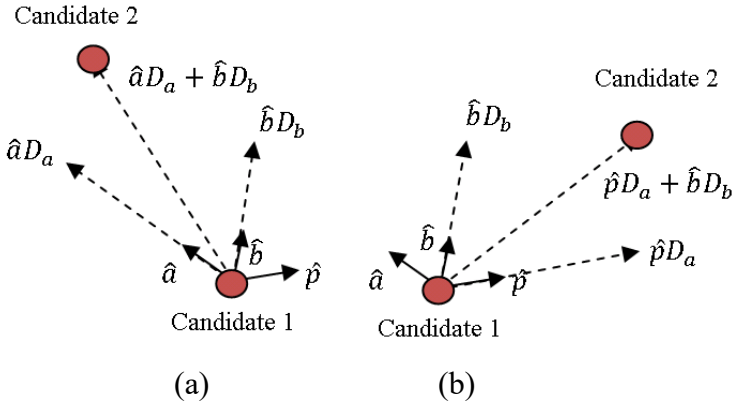

Fig. 2.4. Search progression, reprinted for cases when (a) Candidate 1 is outside the ACPR acceptable region and (b) Candidate 1 is inside the ACPR acceptable region. Reprinted from [23].

The specific method discussed in the previous paragraph was first published by a previous member of the research group [23]. This thesis presents some changes to this optimization that are aimed at improving it but keeps the principles that were initially established.

2.2.2 State of the Art in Circuit Optimization

This section contains an overview of the latest and past work in circuit optimization. The quintessential principles of Pareto optimization are shown in [24]. There are also other papers that involve Pareto optimization between two variables [25-30]. Sevic shows the dependence of PAE and ACPR on Γ_L[31]. Raab talks about the amplifier non-linearity due to distortion [32].

Multiple methods for load impedance optimization have been tested including fuzzy control [33], neural network [34], and least-squares [35]. A search using a simplex and pattern search have also been explored [36]. There have been several algorithms presented to optimize using a gradient based method that was described above on the Smith Chart [37-38]. There have also been papers describing this gradient-based method in the Smith Tube including the Bandwidth, Power, and Bias Smith Tube [39-41]. Qiao demonstrated amplifier optimization using varactors and MEMS switches over a frequency range [42]. Sun proposes several ideas for a cognitive radio system and connects adaptive impedance tuning with high efficiency transmitter operation [43].

2.3 Background of Impedance Tuners

Varactors function as variable capacitors. They are reverse biased P-N junction diodes that take advantage of the separation between the P and N nodes. These two

regions can be likened two the two plates on a capacitor. When the reverse bias across the diode is increased, the depletion region between these two regions is increased. This is equivalent to pulling the plates of a capacitor apart which would result in capacitance decreasing [44].

A matching network serves as a way of matching a load impedance to an input impedance resulting in maximum output power. This is achieved by using inductors and capacitors in parallel or series. This concept can easily be illustrated on the Smith Chart that displays both impedance and admittance called the ZY Smith Chart. The addition of series reactive components causes travel along constant resistance circles, while the addition of shunt reactive components causes travel along constant conductance circles. Inductive components cause travel upward along a constant resistance or conductance circle. Capacitive components cause downward travel. It can be illustrated that any matching combination to provide an impedance with a nonzero real component can be achieved with two components from any other impedance with a nonzero real component, and there are often multiple ways to achieve the same match at the design frequency. However, when designing a dynamic matching network, it can be more useful to have a three component matching network because it may yield better Smith Chart coverage. Figure 2.5 shows an example of Smith Chart traces for a three-element matching network in a “Tee” configuration.

The matching network used for the experiments in this paper was fabricated previously based of a design by Fu and Mortazawi [45]. It is a Tee network with three varactors in series and a varactor and an inductor in shunt. Since variable inductors do not exist, a varactor was added in series to the inductor in shunt in order to give it dynamic

behavior. This results in a component whose net behavior is very similar to an inductor.

A layout of the matching network is shown in Figure 2.6.

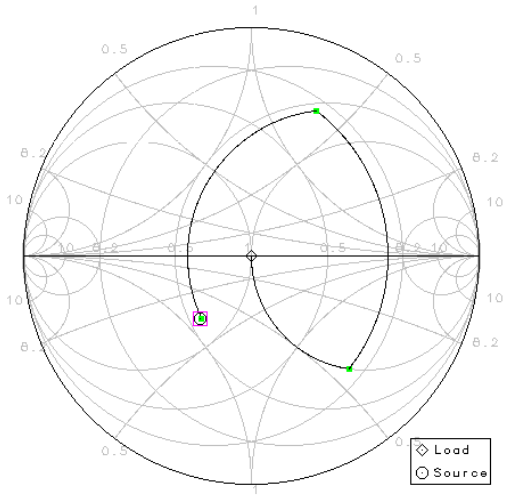

Figure 2.5. Example of traces for a matching network

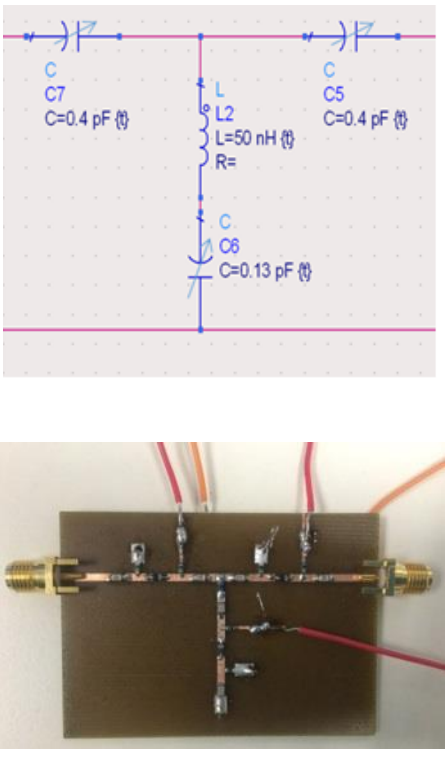

Figure 2.6. (a) Circuit schematic of RF components and (b) layout of the varactor matching network

Three power supplies ranging from 0-30 V were connected to the varactor. The matching network operates at 1.3 GHz, and it can cover about 60-70 % of the Smith Chart. A characterization of the tuner plotted on the Smith Chart is shown in Figure 2.7 to illustrate the coverage of the tuner. A characterization is when a large variety of combinations for the biasing of the varactors is tested, and the resulting impedance is recorded onto a table that can be referenced later when a desired Γ_L is requested.

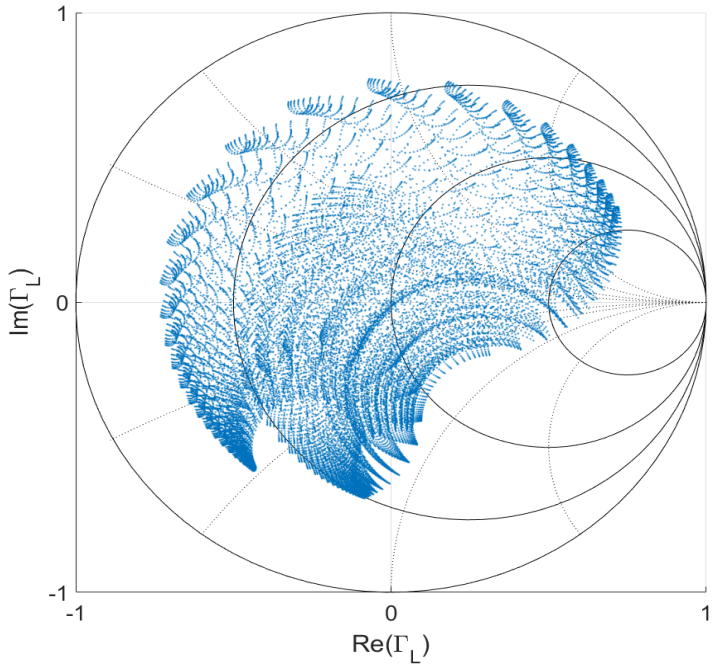

Figure 2.7. Typical Charcterization of the Varactor Tuner

The evanescent-mode resonant cavity tuner consists of two individual tuning elements [46]. The resonant frequency is adjusted by controlling the piezoelectric disc which changes the air gap over the resonator posts. Figure 2.8 shows the layout of the tuner. The change in resonant frequency results in a change in Γ_L. This tuner is capable of handling over 90 W of power which makes it ideal for use in radar test bench. It has about 30% bandwidth, which makes it useful when changing frequency while optimizing.

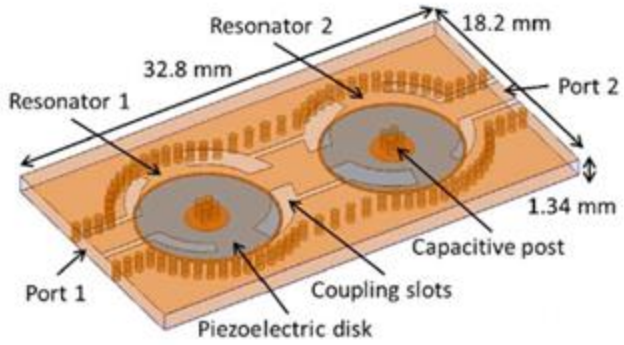

Figure 2.8. Layout of the employed evanescent-mode cavity tuner. Reprinted from [46].

The resonant cavity is controlled by a field-programmable gate array (FPGA) that runs a control loop. The control loop uses a counter that is proportional to the monitored resonant cavity position. There is also a comparator in place that compares the number obtained from the resonant position counter to a number that represents the target position. The output of the comparator triggers a charge pump controller that converts its output into a voltage that is applied to the membrane of the resonators. The controller ensures a deterministic control of the tuner that negates any hysteric or creeps that can be introduced by a piezoelectric actuator. This ensures repeatability when resonant cavity position numbers are input into the controller. Figure 2.10 shows a typical characterization of this tuner.

The two impedance tuners discussed in this section are not necessarily the focus of this thesis. Working with these tuners to implement circuit optimization for a cognitive radar is the primary focus of this thesis. There has been some previous work in taking preliminary measurements with the varactor tuner [46]. This thesis will show detailed results exploring constrained circuit optimization using this varactor network with new techniques. There has also been work using the resonant cavity tuner for constraint

optimization on the Smith Chart by a member of my research group Luci Hays, but this thesis presents an alternative way of performing these optimization that presents multiple advantages.

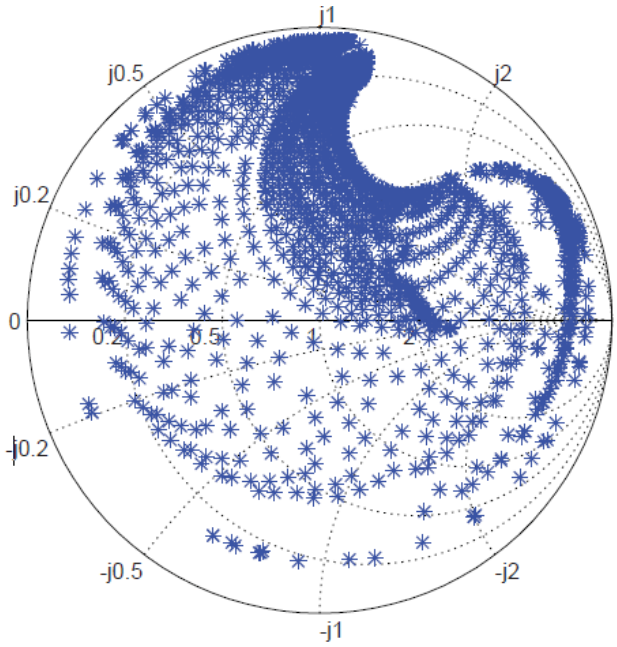

Figure 2.10. Typical characterization of the resonant cavity tuner. Reprinted from [46].

2.3.2 State of the Art in Impedance Tuners

There has been some recent development in the area of high-power tunable devices. There has been some previous literature about the resonant cavity tuner presented in this thesis [48-50]. There has also been development with the use of plasma devices as resonators [51].

The idea of using a look-up table for tuning an adaptive impedance matching network has been used before [52]. Deve shows the development of an impedance matching network with MEMS switches that operates from 1-3 GHz [53]. Nemati explores the design and nonlinearities of a varactor network which is caused by variation

of capacitance values due to large-signal modulation [54]. Shen attempts to use two-tone intermodulation to measure non-linearity in RF-MEMS varactors [55]. Hoarau and Meyer show efforts to model and assess nonlinearity in a varactor network [56-57]. Park shows third-order intermodulation products as a function of varactor bias voltage [58]. Buisman shows the efforts to mitigate nonlinearity by placing anti-series and anti-parallel combinations [59].

CHAPTER THREE

Real-Time Load-Impedance Amplifier Optimization Using a Non-Linear Tunable Varactor Network

This chapter has been accepted for publication as [2] S. Rezayat, C. Kappelmann, Z. Hays, L. Lamers, C. Baylis, E. Viveiros, A. Hedden, J. Penn, and R. Marks II. "Real-Time Amplifier Load-Impedance Optimization for Adaptive Radar Transmitters Using a Nonlinear Tunable Varactor Matching Network," *IEEE Transactions on Aerospace and Electronic Systems,* 2018.

Anticipated challenges with real-time optimization using the varactor matching network included reducing time per measurement and handling non-idealities of the network. For certain Γ_L values, the S-parameters of the varactor network change significantly with input power, as shown in Figure 3.1. Figure 3.2 shows a small-signal characterization in blue with 0 dBm of input power with a characterization with 14 dBm of input power plotted on top in green. It is apparent that the characterized values of Γ_L can change significantly with input power. Additionally, the S-parameters of the varactor network possess a significant frequency dependence. Therefore, the bandwidth of the excitation waveform was changed to 60 kHz from 70 MHz to mitigate this issue.

Alleviating the nonlinearity in respect to power was a much more challenging issue. The characterization of the tuner changes with respect to input power. Therefore, multiple characterizations were taken ranging from 0 to 14 dBm of input power with 1 dBm steps. In order to allocate the use of the correct characterization, output power of the device under test must be known. However, the calculation of output power is dependent on the characterization since the S-parameters recorded in the characterization are required to correctly de-embed output power. Therefore, an iterative process was

invented that initially calculates output power with an initial guess. For the data shown in this thesis, this original guess was always 0 dBm except when a number of measurements were taken consecutively in which case the guess carries over form the last measurement taken. Using this guess, the output power of the device under test (DUT) is measured and the characterization guess is changed to this output power. Then another measurement is taken that uses this new characterization guess. If the new output power calculated is within a set limit then the algorithm stops. Otherwise, this process will continue until the limit is reached. Figure 3.3 shows a block diagram of this process. For the measurements taken in this thesis this limit is 0.5 dBm.

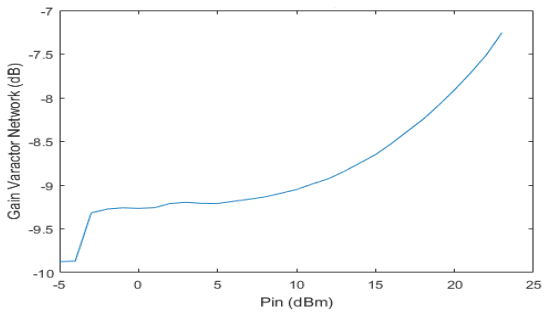

Figure 3.1. Measured $|S_{21}|$ versus input power for the varactor matching network at $\Gamma_L = 0.7/\underline{90°}$

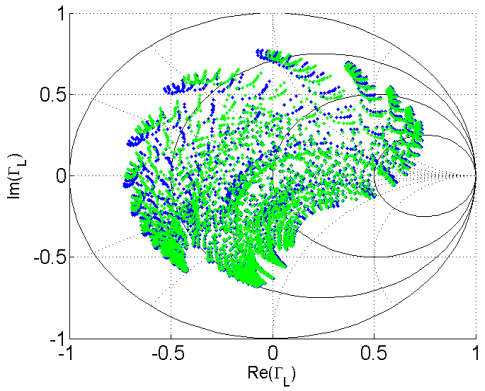

Figure 3.2. Tuner chracterization at large-signal (green) and small-signal (blue)

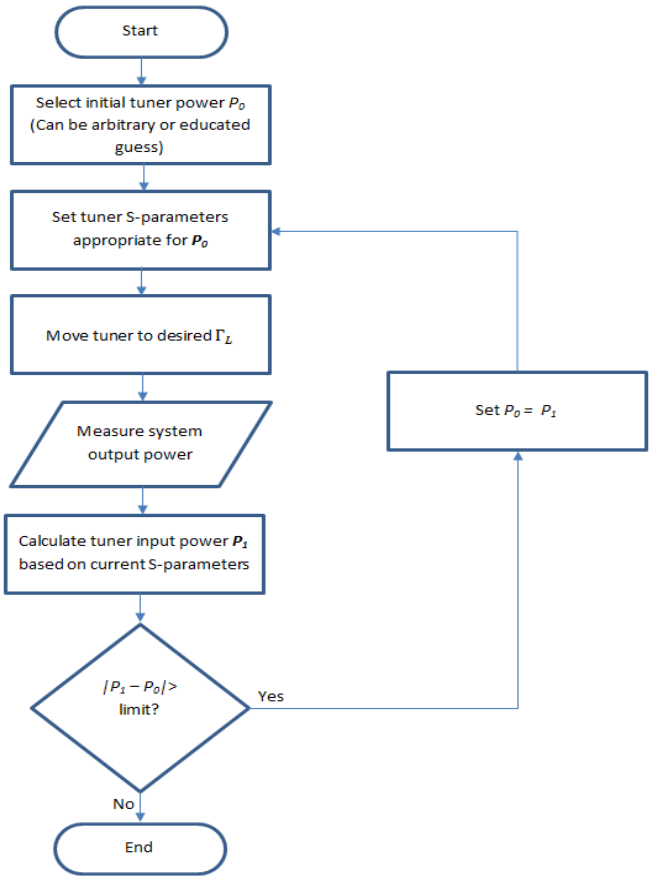

Figure 3.3. Process flow of the characterization choosing algorithm

This approach was measurement tested using a Microwave Technologies MWT-173 field-effect transistor (FET). It was tested under two conditions. The first test condition was with P_{in} = 5 dBm, V_{GS} = -1.5 V, and V_{DS} = 3. The design frequency for the varactor tuner is 1.3 GHz, and this was used as the operating frequency for all the measurements in this section. A traditional load-pull was taken with a mechanical tuner, which served as the standard to which the other load-pulls could be compared. These results are shown in Figure 3.4. The basic setup of the test bench used for these measurements is shown in Figure 3.5.

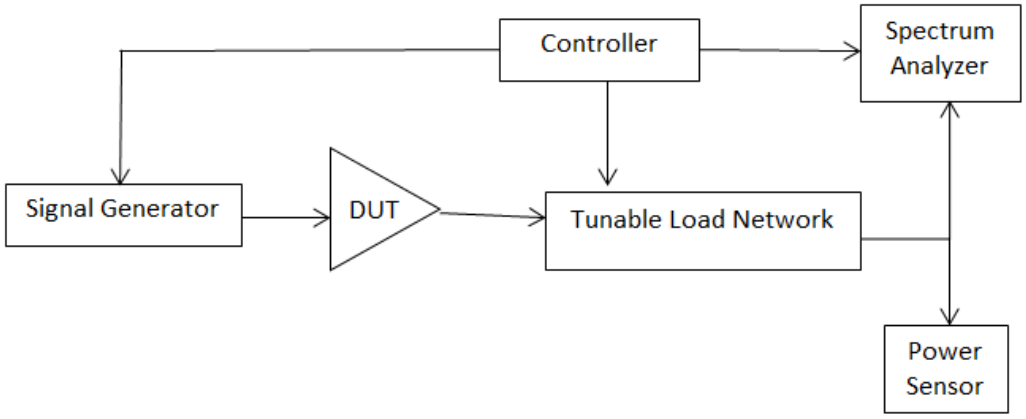

Figure 3.4. Test bench setup

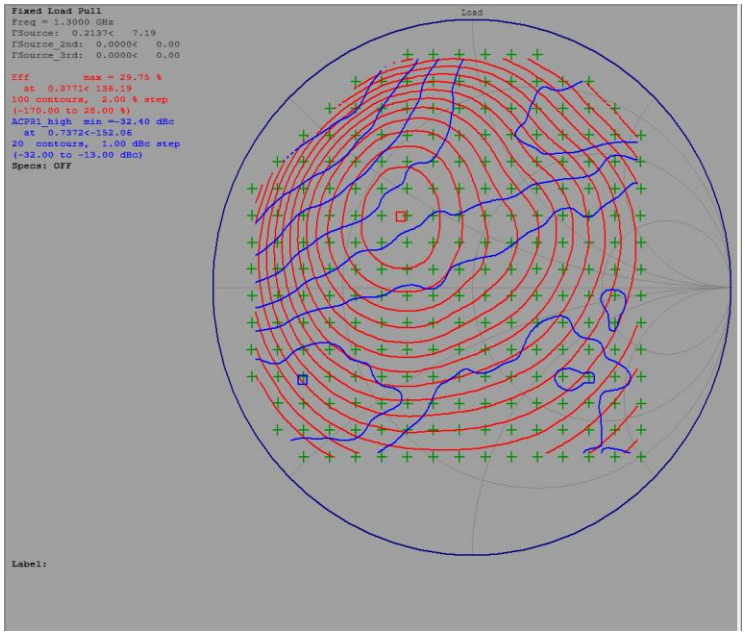

Figure 3.5. MWT-173 PAE (red) and ACPR (blue) contours for V_{GS} = -1.5 V, V_{DS} = 3 V, and P_{in} = 5 dBm measured with a Maury Microwave mechanical tuner

These same measurements were then taken with the varactor tuner in place of the mechanical tuner. Initially, these measurements were taken with a small-signal characterization using an input power of 0 dBm. Figure 3.6 shows these results. A power-

dependent characterization was then used to perform the same measurements, as shown in Figure 3.7.

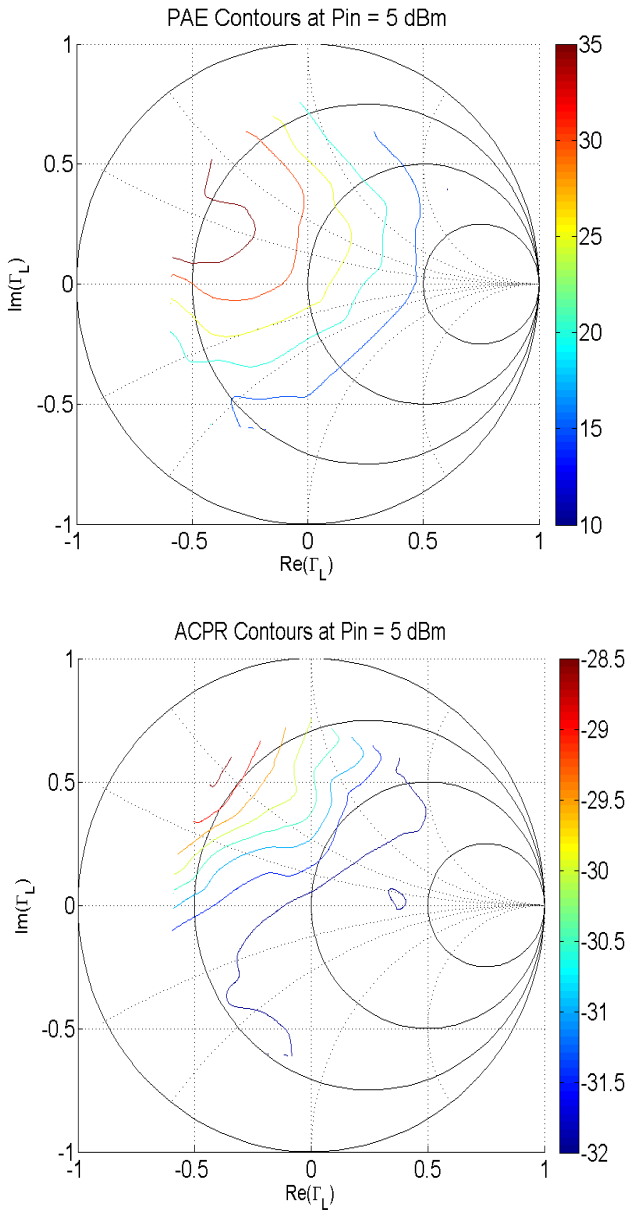

Figure 3.6. MWT-173 PAE (top) and ACPR (bottom) contours for V_{GS} = -1.5 V, V_{DS} = 3 V, and P_{in} = 5 dBm measured with the tunable-varactor matching network based on a small-signal characterization

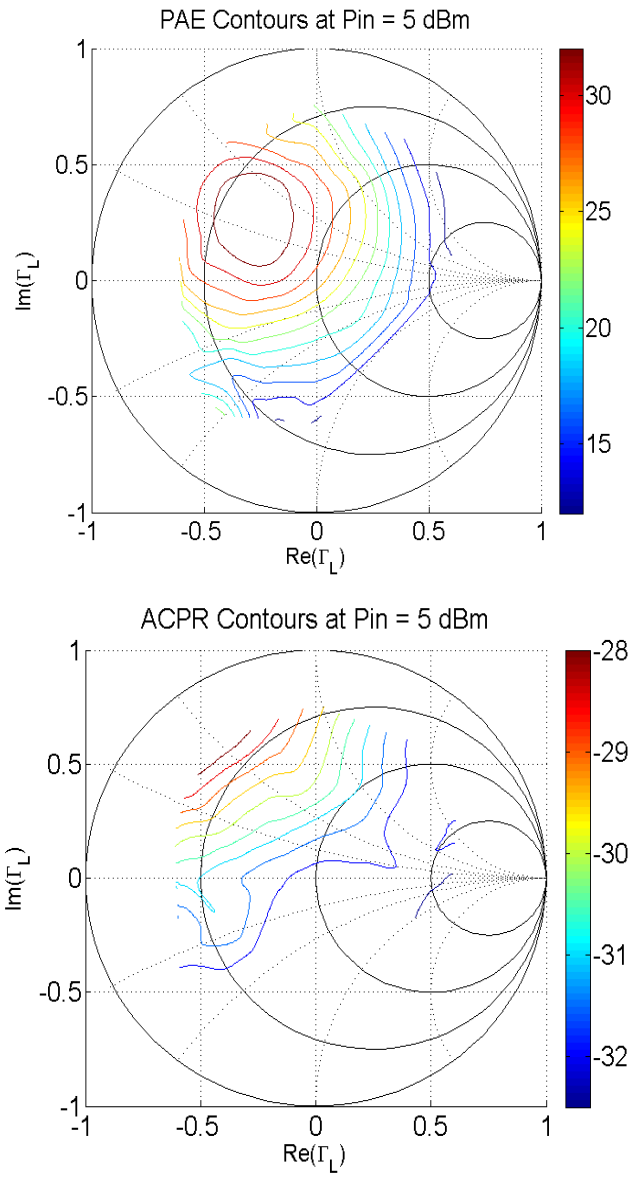

Figure 3.7. MWT-173 PAE (top) and ACPR (bottom) contours for V_{GS} = -1.5 V, V_{DS} = 3 V, and P_{in} = 5 dBm measured with the tunable-varactor matching network based on a power-dependent characterization.

The power-dependent characterization corrects several issues that are encountered in measurements using a small-signal characterization. First, the PAE of the small-signal load-pull is larger than what it should be. This is because as input power increases, $|S_{21}|$ also typically increases. This results in both output power and PAE being reported higher

when the system is de-embedded using a characterization that is too low. Additionally, the location of the PAE optimum is closer when using the power-dependent characterization. The contours also tend to look smoother, which is a result of a more accurate characterization.

The same experiment was performed for a second condition of the transistor: V_{GS} = -1 V,$V_{DS} = 2\ V$, and $P_{in} = 4$ dBm. Figure 3.8 shows a load-pull taken with a mechanical tuner. Figure 3.9 shows a load-pull taken with a small-signal characterization. Figure 3.10 shows a load-pull taken with a power-dependent characterization. The contours are much smoother when using the small-signal characterization. The PAE values are also closer to the ones obtained by the mechanical tuner.

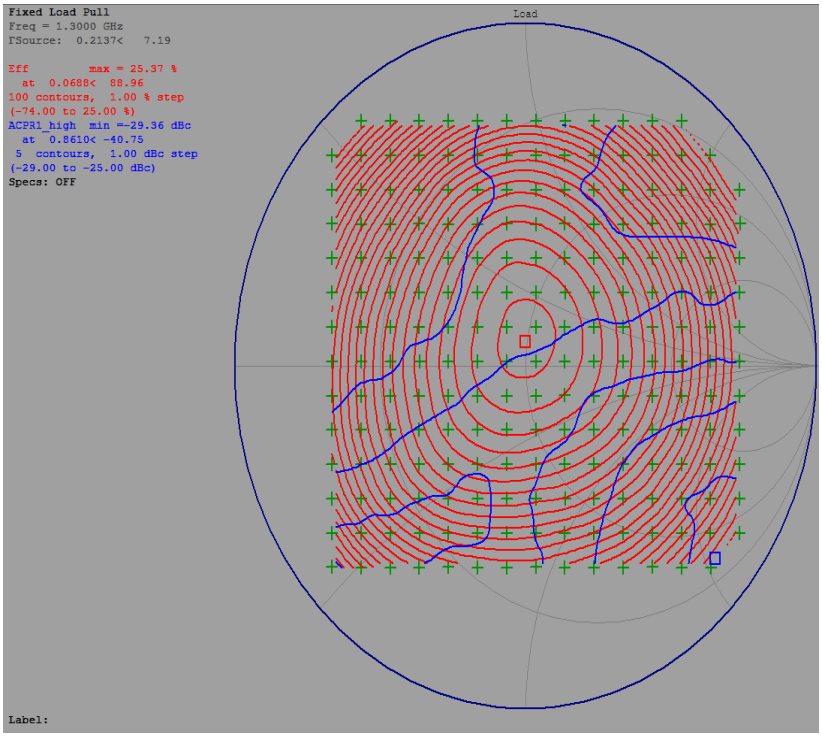

Figure 3.8. MWT-173 PAE (red) and ACPR (blue) contours for V_{GS} = -1 V, $V_{DS} = 2$ V, and $P_{in} = 4$ dBm measured with a Maury Microwave mechanical tuner

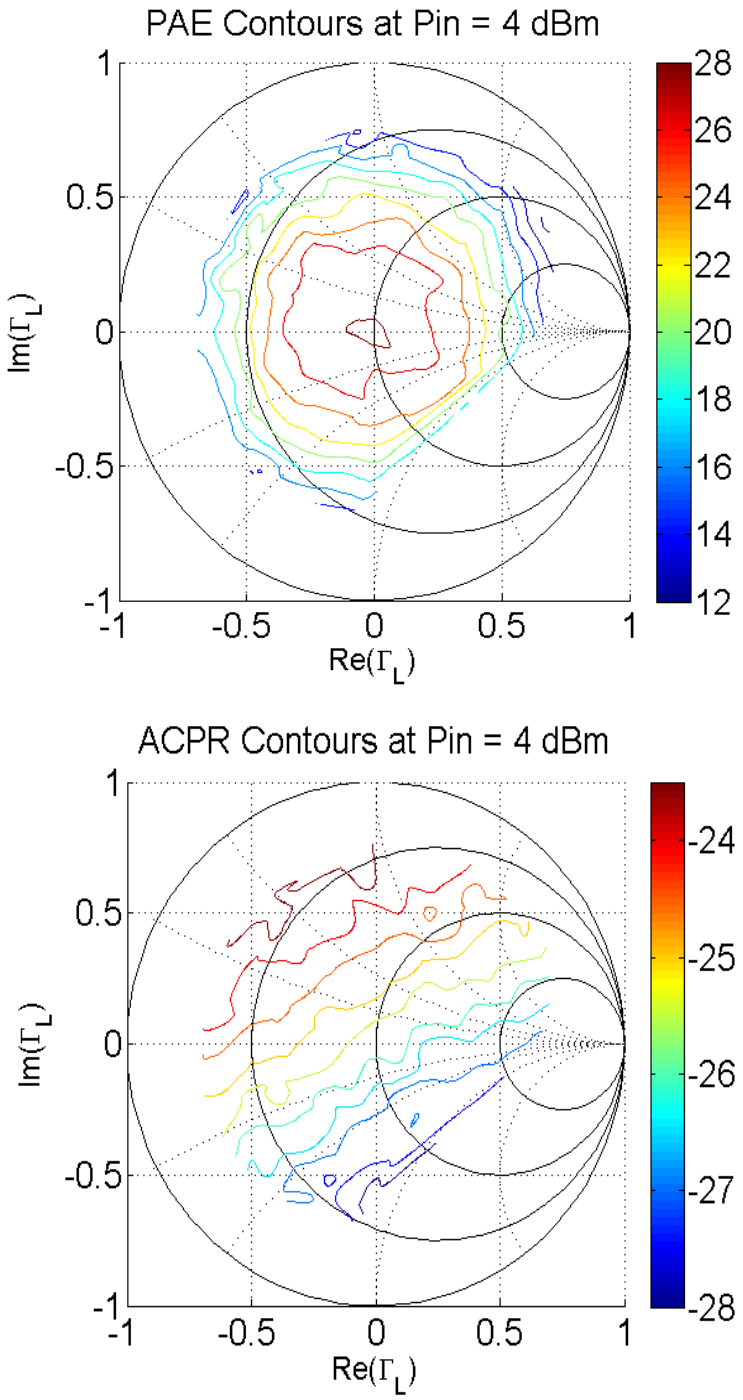

Figure 3.9. PAE (top) and output power (bottom) contours for V_{GS} = -1 V, V_{DS} = 2 V, and P_{in} = 4 dBm measured with the tunable-varactor matching network based on a small-signal characterization

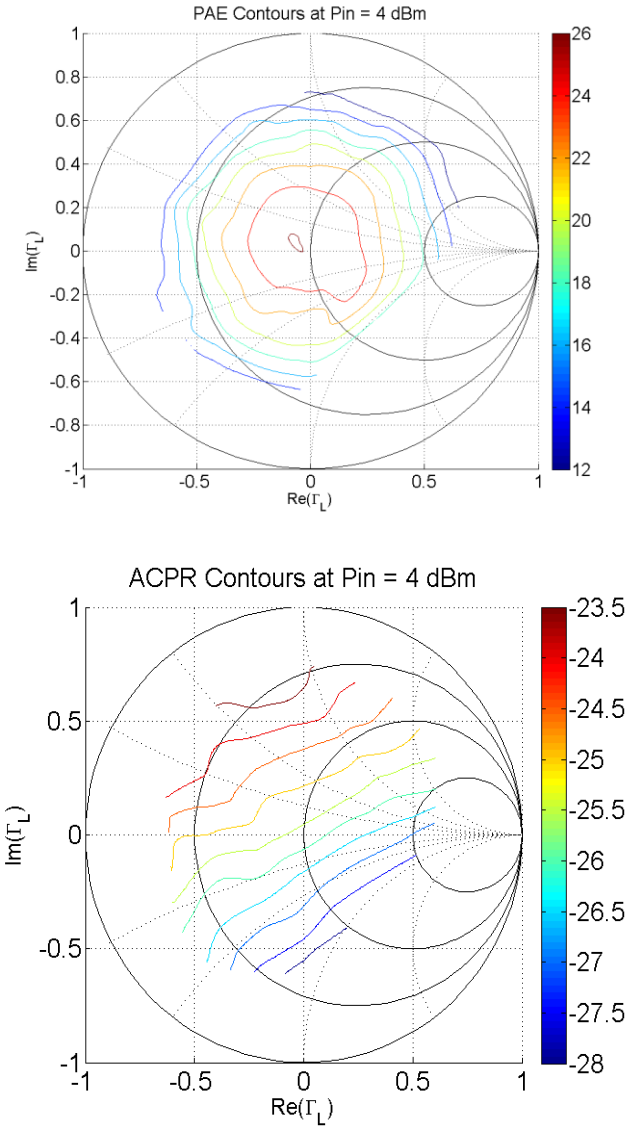

Figure 3.10. PAE (top) and output power (bottom) contours for V_{GS} = -1 V, V_{DS} = 2 V, and P_{in} = 4 dBm measured with the tunable-varactor matching network based on a power-dependent characterization

Constrained optimum searches were performed using the three different methods as well. An initial search was performed using a mechanical tuner under the first condition which is P_{in} = 5 dBm, V_{GS} = -1.5 V, and V_{DS} = 3. The ACPR limit for this search was -30.5 dBc. For the searches using the mechanical tuner, the average end PAE value is 30.07% with a standard deviation of 0.78% PAE. The average number of

measurements is 12.25 with each measurement taking 17.32 seconds on average. Table 3.1 contains the results of these searches. Start locations are spread out across the Smith Chart to ensure that the search converges from anywhere. The data shows that regardless of start location the search still converges to a similar end location and PAE value.

TABLE 3.1: SEARCH ALGORITHM RESULTS USING THE MECHANICAL TUNER FOR $V_{GS} = -1.5$ V, $V_{DS} = 3\,V$, $P_{in} = 5$ dBm

Start Γ_L	Start PAE (%)	End Γ_L	End ACPR	End PAE (%)	# Meas
0/0°	24.79	0.24/154°	-31.10	29.98	9
0.25/0°	16.17	0.27/154°	-30.69	28.43	15
0.25/45°	23.33	0.23/156°	-30.74	27.67	12
0.25/90°	26.78	0.23/142°	-30.97	30.12	13
0.25/-45°	16.70	0.30/149°	-30.68	30.73	15
0.25/-90°	17.02	0.26/138°	-30.68	30.51	11
0.25/135°	30.30	0.28/151°	-3061	30.44	9
0.25/180°	27.93	0.28/149°	-30.54	30.54	9
0.25/-135°	21.86	0.28/155°	-30.57	30.20	10
0.5/0°	11.82	0.22/141°	-30.67	29.80	16
0.5/45°	16.80	0.29/147°	-30.63	30.65	15
0.5/90°	23.68	0.28/143°	-30.53	30.69	13
0.5/-135°	14.97	0.27/159°	-30.85	29.92	10
0.5/-90°	8.34	0.24/148°	-30.56	30.23	14
0.5/135°	30.27	0.27/148°	-30.67	30.55	16
0.5/180°	24.35	0.34/159°	-30.50	30.22	9

This search was then performed using a small-signal characterization. The data summary is Table 3.2. For these measurements, the average end PAE value found is 34.32%, with 2.25% PAE standard deviation. The average number of measurements is 12.88, with an average time per measurement of 4.28 seconds. Table 3.3 contains the data from searches run with the power-dependent characterization. For these measurements, the average end PAE value found is 32.30%, with 1.40% PAE standard deviation. The average number of measurements is 13.31, with average time per

measurement of 3.70 seconds. Figures 3.11 and 3.12 shows examples of searches. The search that uses the power-dependent takes a more direct path while the one that uses the small-signal characterization zigzags and takes missteps.

Table 3.4 contains a summary of all the searches for comparison. As expected, the number of measurements for the power-dependent search is higher since more measurements have to be taken to determine the power level of the characterization that needs to be used. Notably, the number of measurements in only marginally larger for the power-dependent search since the search converges more easily. One of the biggest differences between these results is that the searches performed using the power-dependent characterization have a much smaller standard deviation. This is because the search converges much more consistently when the appropriate characterization is used, and it has better repeatability. The search also has a smaller average end PAE value when the power-dependent characterization is used, and the location that it converges to is also closer to the results shown in Table 3.1 with the traditional tuner. This is again due to the characterization S-parameters being more inaccurate when only the small signal characterization is used.

In order to thoroughly test the algorithm, the search was also tested with another bias condition. The transistor was biased to V_{GS} = -1 V, $V_{DS} = 2\ V$, and $P_{in} = 4$ dBm. The load-pulls at this bias were shown earlier in this section as a reference. Table 3.5, 3.6, and 3.7 show the results from the search algorithms. Table 3.8 contains the summary of these searches. Figure 3.13 and 3.14 show examples of these searches. The results again show an improvement when using the power-dependent characterization. When the power-dependent characterization is used, the search converges more consistently which

is exemplified by the lower standard deviation. The values of PAE obtained by this search are also more comparable to the ones obtained by the search using the mechanical tuner.

TABLE 3.2: SEARCH ALGORITHM RESULTS USING SMALL-SIGNAL MATCHING NETWORK CHARACTERIZATION FOR V_{GS} = -1.5 V, $V_{DS} = 3\,V$, P_{in} = 5 dBm

Start Γ_L	Start PAE (%)	End Γ_L	End ACPR (dBc)	End PAE (%)	# Meas.
0/0°	27.93	0.35/156°	-30.75	36.78	11
0.25/0°	21.66	0.37/115°	-30.66	32.99	13
0.25/45°	26.17	0.33/134°	-30.57	36.43	18
0.25/90°	28.72	0.27/118°	-30.99	33.08	9
0.25/-45°	19.05	0.37/148°	-30.63	37.77	27
0.25/-90°	19.20	0.37/126°	-30.65	36.52	10
0.25/135°	32.54	0.33/122°	-30.93	35.33	8
0.25/180°	29.86	0.33/144°	-30.9	36.05	17
0.25/-135°	24.85	0.41/163°	-30.94	34.63	10
0.5/0°	13.93	0.28/44°	-32.12	25.1	9
0.5/45°	19.51	0.35/135°	-30.71	33.85	14
0.5/90°	28.73	0.44/92°	-30.61	29.23	4
0.5/-135°	18.92	0.37/151°	-31.04	35.07	7
0.5/-90°	13.68	0.33/160°	-31.18	35.00	31
0.5/135°	37.12	0.36/141°	-30.68	36.33	12
0.5/180°	30.76	0.43/157°	-30.79	36.22	8

TABLE 3.3: SEARCH ALGORITHM RESULTS USING POWER-DEPENDENT MATCHING NETWORK CHARACTERIZATION FOR V_{GS} = -1.5 V, $V_{DS} = 3\,V$, P_{in} = 5 dBm

Start Γ_L	Start PAE (%)	End Γ_L	End ACPR	End PAE (%)	# Meas
0/0°	26.11	0.37/156°	-30.87	32.44	15
0.25/0°	18.69	0.29/139°	-31.02	32.28	14
0.25/45°	22.42	0.35/125°	-30.54	32.68	16
0.25/90°	28.50	0.26/130°	-30.94	31.96	15
0.25/-45°	18.42	0.27/152°	-31.20	31.93	14
0.25/-90°	18.37	0.41/165°	-31.02	31.30	14
0.25/135°	31.25	0.33/122°	-30.79	31.69	7
0.25/180°	28.16	0.25/128°	-30.85	31.98	7
0.25/-135°	23.79	0.29/136°	-30.85	32.33	14
0.5/0°	12.15	0.28/138°	-30.90	32.25	20
0.5/45°	17.99	0.25/133°	-31.21	32.09	12
0.5/90°	26.06	0.32/133°	-30.76	31.73	16
0.5/-135°	16.46	0.31/139°	-30.76	32.31	16
0.5/-90°	12.80	0.34/131°	-30.70	31.94	16
0.5/135°	32.06	0.26/155°	-31.37	31.91	9
0.5/180°	27.25	0.33/154°	-30.85	32.13	8

TABLE 3.4: COMPARISON OF SEARCH STATISTICS FOR V_{GS} = -1.5 V, $V_{DS} = 3\,V$, P_{in} = 5 dBm

	Varactor Network: Power-Dependent Characterization	Varactor Network: Small-Signal Characterization	Mechanical Tuner
Average End PAE (%)	32.06	34.40	30.07
End PAE Standard Deviation (%)	0.33	3.2	0.78
Average End ACPR (dBc)	-30.91	-30.97	-30.69
Average End Γ_L	0.29/141°	0.35/134°	0.27/149°
Average Time Per Measurement (seconds)	4.4	4.28	17.32
Average Number of Measurements	13.31	13	12.25

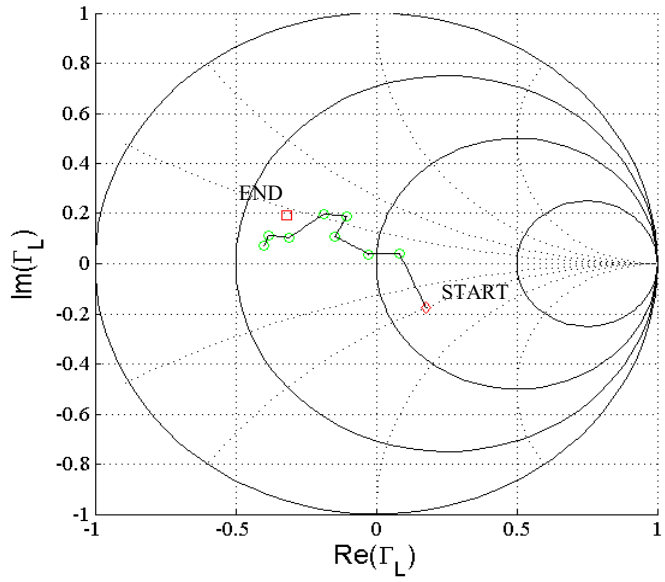

Figure 3.11. Search trajectory on the Smith Chart with starting $\Gamma_L = 0.25\angle{-45°}$ to find the highest PAE with ACPR ≤ -30.5 dBc with a small-signal matching-network characterization. Device conditions are $V_{GS} =$ -1.5 V, $V_{DS} = 3$ V, and $P_{in} = 5$ dBm.

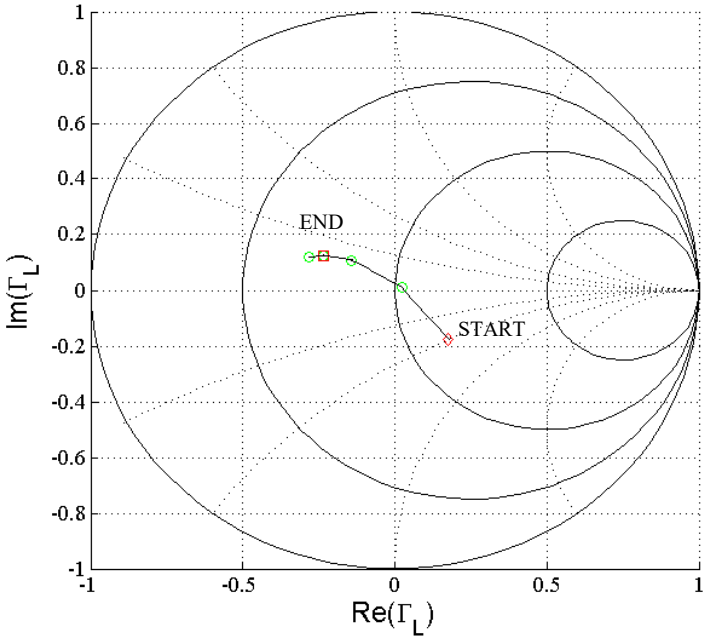

Figure 3.12. Search trajectory on the Smith Chart with starting $\Gamma_L = 0.25\angle{-45°}$ to find the highest PAE with ACPR ≤ -30.5 dBc using a power-dependent matching-network characterization. Device conditions are $V_{GS} =$ -1.5 V, $V_{DS} = 3$ V, and $P_{in} = 5$ dBm

TABLE 3.5: SEARCH ALGORITHM RESULTS USING THE MECHANICAL TUNER FOR V_{GS} = -1 V, $V_{DS} = 2\,V$, $P_{in} = 4$ dBm

Start Γ_L	Start PAE (%)	End Γ_L	End ACPR	End PAE (%)	# Meas
0/0°	25.15	0.26/-24°	-27.07	22.44	10
0.25/0°	23.07	0.27/-30°	-27.19	22.14	12
0.25/45°	23.70	0.24/-35°	-27.12	22.60	22
0.25/90°	24.37	0.30/-10°	-27.05	22.04	16
0.25/-45°	22.06	0.25/-45°	-27.08	22.06	5
0.25/-90°	21.62	0.24/-44°	-27.21	22.18	12
0.25/135°	23.36	0.29/-19°	-27.07	22.07	19
0.25/180°	22.65	0.33/-105°	-27.02	20.29	22
0.25/-135°	22.54	0.24/-60°	-27.13	21.89	10
0.5/0°	17.27	0.23/-29°	-27.11	22.74	14
0.5/45°	17.60	0.39/-14°	-27.24	19.75	13
0.5/90°	19.63	0.23 /-36°	-27.06	22.26	31
0.5/-135°	15.73	0.36/-109°	-27.02	18.18	9
0.5/-90°	14.87	0.27/-44°	-27.15	21.63	8
0.5/135°	17.10	0.23/-34°	-27.11	22.53	31
0.5/180°	14.84	0.24/-34°	-27.15	21	16

TABLE 3.6: SEARCH ALGORITHM RESULTS USING SMALL-SIGNAL MATCHING NETWORK CHARACTERIZATION FOR V_{GS} = -1 V, $V_{DS} = 2\,V$, $P_{in} = 4$ dBm

Start Γ_L	Start PAE (%)	End Γ_L	End ACPR (dBc)	End PAE (%)	# Meas.
0/0°	28.31	0.26/-56°	-27.13	24.06	7
0.25/0°	26.36	0.32/-32°	-27.40	25.29	13
0.25/45°	26.87	0.32/-34°	-27.50	25.29	16
0.25/90°	25.99	0.28/-50°	-27.18	25.55	11
0.25/-45°	24.9	0.32/-34°	-27.41	25.28	15
0.25/-90°	23.96	0.34/-30°	-27.62	24.93	12
0.25/135°	26.21	0.31/-59°	-27.22	24.48	10
0.25/180°	26.04	0.21/-59°	-27.15	24.84	7
0.25/-135°	26.14	0.29/-92°	-27.18	23.20	7
0.5/0°	19.66	0.29/-45°	-27.17	25.65	14
0.5/45°	21.12	0.54/1°	-27.21	18.09	13
0.5/90°	21.56	0.39/-10°	-27.23	23.54	17
0.5/-135°	20.38	0.36/-99°	-27.24	23.38	10
0.5/-90°	19.43	0.40/-98°	-27.27	22.51	9
0.5/135°	22.77	0.23/-60°	-27.34	24.18	16
0.5/180°	21.49	0.46/-109°	-27.22	21.20	16

TABLE 3.7: SEARCH ALGORITHM RESULTS USING POWER-DEPENDENT MATCHING NETWORK CHARACTERIZATION FOR V_{GS} = -1 V, $V_{DS} = 2\,V$, $P_{in} = 4$ dBm

Start Γ_L	Start PAE (%)	End Γ_L	End ACPR	End PAE (%)	# Meas
0/0°	28.26	0.23/-36°	-27.08	25.09	10
0.25/0°	25.22	0.31/-28°	-27.20	24.44	7
0.25/45°	25.67	0.28/-42°	-27.26	25.50	10
0.25/90°	26.42	0.30/-50°	-27.42	24.94	13
0.25/-45°	25.10	0.25/-45°	-27.05	25.10	4
0.25/-90°	25.56	0.22/-40°	-27.04	25.72	12
0.25/135°	26.62	0.24/-66°	-27.36	24.48	10
0.25/180°	26.29	0.24/-72°	-27.22	24.80	7
0.25/-135°	26.02	0.31/-46°	-27.55	24.96	10
0.5/0°	18.82	0.24/-38°	-27.07	25.02	17
0.5/45°	21.14	0.25/-36°	-27.02	25.12	13
0.5/90°	21.33	0.34/-16°	-27.02	24.38	16
0.5/-135°	20.03	0.34/-99°	-27.24	24.28	13
0.5/-90°	19.78	0.34/-92°	-27.06	24.40	7
0.5/135°	19.14	0.26/-95°	-27.03	24.21	16
0.5/180°	19.96	0.33/-93°	-27.12	24.37	13

TABLE 3.8: COMPARISON OF SEARCH STATISTICS FOR V_{GS} = -1 V, $V_{DS} = 2\,V$, $P_{in} = 4$ dBm

	Varactor Network: Large-Signal Characterization	Varactor Network: Small-Signal Characterization	Mechanical Tuner
Average End PAE (%)	24.80	23.84	21.61
End PAE Standard Deviation (%)	0.45	1.96	1.23
Average End ACPR (dBc)	-27.12	-27.28	-27.11
Average End Γ_L	0.25/-55°	0.31/-63°	0.24/-42°
Average Time Per Measurement (seconds)	4.29	4.86	19.23
Average Number of Measurements	11.12	12.06	15.62

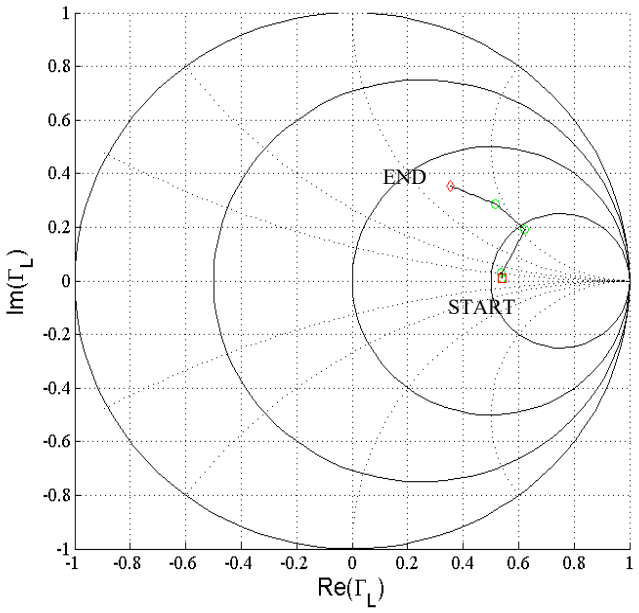

Figure 3.13. Search trajectory on the Smith Chart with starting $\Gamma_L = 0.5\angle 45°$ to find the highest PAE with ACPR ≤ -27 dBc with a small-signal matching-network characterization. Device conditions are V_{GS} = -1 V, V_{DS} = 2 V, and P_{in} = 4 dBm.

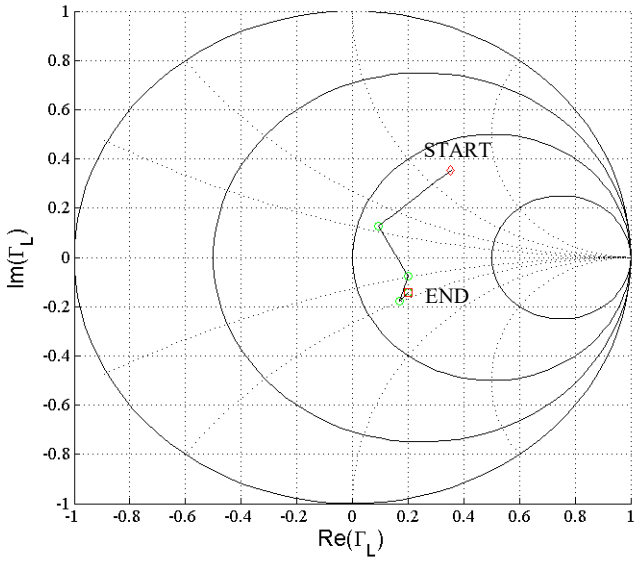

Figure 3.14. Search trajectory on the Smith Chart with starting $\Gamma_L = 0.5\angle 45°$ to find the highest PAE with ACPR ≤ -27 dBc using a power-dependent matching-network characterization. Device conditions are V_{GS} = -1 V, V_{DS} = 2 V, and P_{in} = 4 dBm.

In conclusion, this chapter demonstrates the use of a varactor matching network in real-time circuit optimization using a power-dependent characterization. An algorithm was developed in order to choose the suitable characterization. Some of the non-ideal behavior of the varactor tuner was mitigated in order to obtain accurate data. The time per measurement was reduced to 3.7 seconds from 16 seconds with a traditional tuner. This takes us closer to a reconfigurable amplifier for a cognitive radar that is able to adapt in real-time as it changes operating conditions to suit the environment around it.

CHAPTER FOUR

Circuit Optimization in the Power Smith Tube Using a Non-Linear Varactor Network

As explained in Chapter three, using the varactor tuning network presented many challenges. One such challenge was expanding the search to the Smith Tube for co-optimization of an additional parameter with load reflection coefficient. There are multiple types of Smith Tubes, but the one that will theoretically present the most challenge is the Power Smith Tube due to non-linearities of the varactor network. Searching in the Power Smith Tube will allow the use of input power as an additional search parameter in the optimization.

An adjustment was made to the power-dependent characterization algorithm to compensate for the large variation in transistor output power (matching network input power) over the range of input power values displayed in the Power Smith Tube. Whenever input power is changed for a measurement, the power guess is also changed by this same amount. Measurement results showed that this does noticeably help reduce the number of measurements required for the power-dependent characterization algorithm to settle.

The first device tested was a packaged Skyworks amplifier. It was biased to $V_{DD} =$ 6.35 V. The range for the Power Tube was determined to be from -9 dBm to 1 dBm. The lower range for the tube was chosen based on the noise floor for ACPR. At approximately -9 dBm, there was no longer any spectral spreading of the amplifier, and therefore the ACPR measurement became only noise. The upper range for the Power

Tube was chosen to be where the device goes into 3 dB of compression, i.e. when the gain of the device is decreased 3 dB from its maximum linear gain. The operating frequency for these measurements was 1.3 GHz.

To provide comparison of the algorithm results to a standard, multiple-power load-pull measurements were performed. Figure 4.1 shows the Power Smith Tube with an ACPR isosurface for -29 dBc plotted in blue. Everything below this surface is the ACPR acceptable region when an ACPR limit of -29 dBc is imposed. The red shape is the PAE isosurface equal to 9.98%, which is the PAE maximum with an ACPR limit of -29 dBc according to the load-pulls taken to construct these plots. These two shapes intersect at one point which is the constrained optimum. According to the data, this particular optimum is located at Γ_L=.32/161.54° and P_{in}=-3 dBm with PAE=9.98% and an ACPR of -29.15 dBc. Figure 4.2 shows the same shapes, but from a different angle with a spotlight feature turned on to show some of the bumpiness in the ACPR isosurface, which could possibly create some issues with the search.

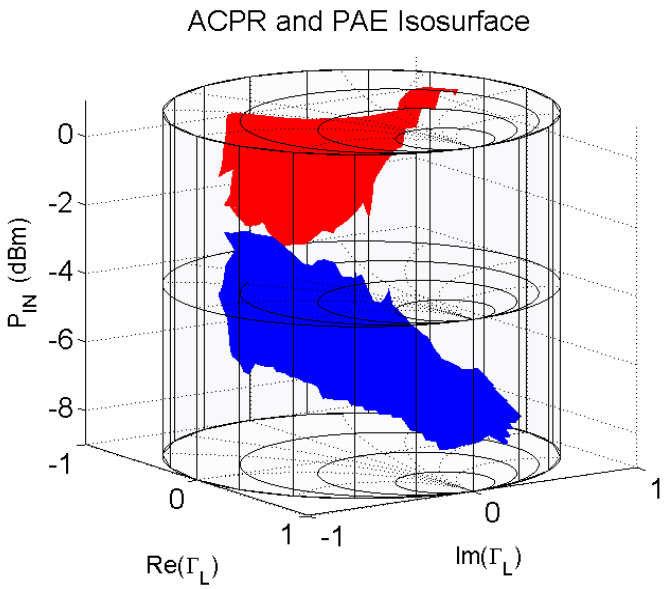

Figure 4.1. The Power Tube for the Skyworks amplifier with a -29 dBc limit

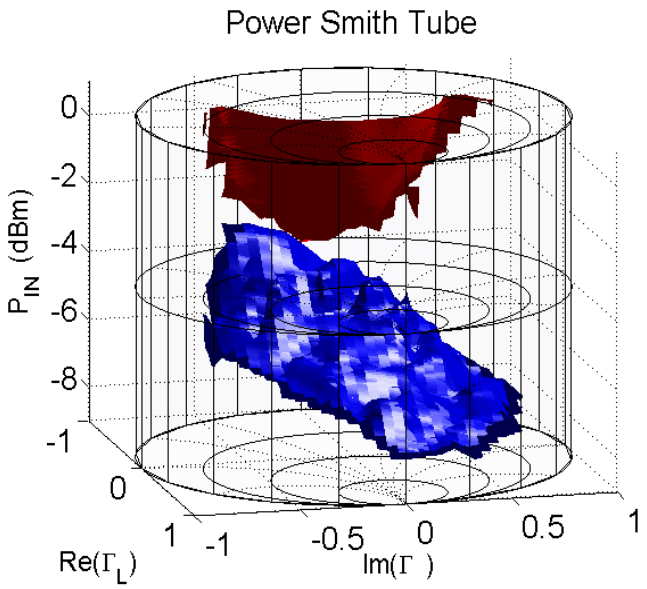

Figure 4.2. The Power Tube figure from a different angle and with different lighting for the Skyworks amplifier

A batch of searches was then performed to test the accuracy and performance of the search when starting at different starting locations throughout the Smith Tube. The results of these searches are shown in Table 4.1. An example of one of the searches is shown in Figure 4.3. The search starts at $P_{in} = -4$ dBm with Γ_L =.5/135°. It ends at Γ_L =.=.47/179.27° with $P_{in} = -1.72$ dBm in 57 measurements with PAE=11.89 and ACPR=-29.04 dBc. The last two rows in the table contains a summary of the searches. The end PAE has a small standard deviation which shows the at the search is efficiently converging. This PAE is also higher in value than the constrained optimum shown in the load-pulls, which is a result of the search having the capacity to have a much finer resolution. The non-convexities of the ACPR acceptable region also does not seem to pose much of an issue, as the end locations of the searches also seem to converge fairly well.

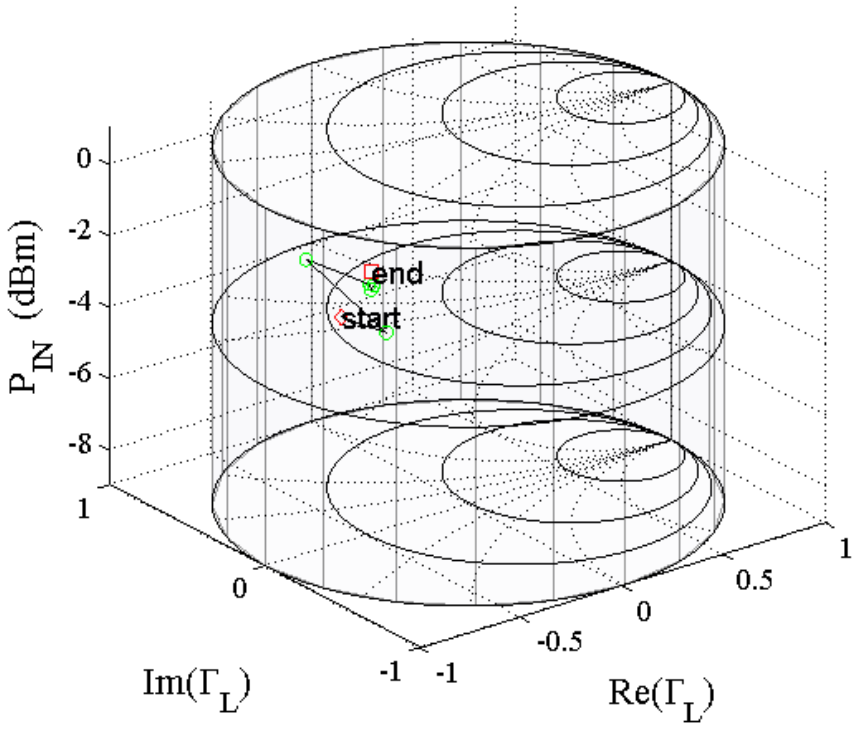

Figure 4.3. Example of a search in the Smith Tube for the Skyworks Amplifier

Another device was tested to confirm that the algorithm was working. This device is the Microwave Technologies MWT-173 FET. The MWT-173 FET was tested with bias V_{GS} = -1 V, V_{DS} = 2 V. The range for the Power Smith Tube was determined to be -6 dBm to 6 dBm. Figure 4.4 shows the Power Smith Tube figures for this device with an ACPR limit of -28 dBc. Figure 4.5 shows the same plot from a different angle and with different lighting. From the load-pull, the constrained optimum is located at Γ_L=.22/-2.75° and $P_{in} = 1\ dBm$ with PAE=26.14% and ACPR=-28.07 dBc.

TABLE 4.1: SEARCH ALGORITHM RESULTS FOR THE SKYWORKS AMPLIFIER FOR $V_{DD} = 6.35\,V$, P_{in} = -9-1 dBm AND $ACPR_{limit} = -29\,dBc$ USING A POWER DEPANDANT CHARCTERIZATION

Start Gamma Real	Start Gamma Imag	Start Pin	Start PAE	End Gamma Mag	End Gamma Theta	End Pin	End ACPR	End PAE	Total Measurements
0	0	-2	8.38	0.49	-178.44	**-2.46**	-29.7	11.53	56
0	0	-4	6.18	0.47	-166.16	-2.1	-29.6	11.45	60
0	0	-6	4.57	0.46	177.52	-1.91	-29.48	11.63	66
0	0	-8	3.16	0.51	-168.65	-2.17	-29.15	**12.03**	67
0	0	0	10.45	0.48	171.48	-2.22	-29.38	11.44	**25**
0.25	0	-2	5.65	0.38	-148.44	**-1.24**	-29.09	**11.26**	49
0.25	0	-6	3.18	0.46	-173.48	-2.01	-29.46	11.74	74
0.25	45	0	7.81	0.37	167.86	-1.95	**-30.18**	**11.27**	80
0.25	45	-4	4.59	0.45	176.12	-1.68	-29.14	11.94	**95**
0.25	45	-8	2.52	0.51	-173.75	-2.14	-29.3	11.83	50
0.25	90	-2	7.49	0.47	-171.43	-2.02	-29.19	11.72	62
0.25	90	-6	4.23	0.44	-154.31	-1.92	-30.12	11.33	42
0.25	-45	0	7.44	0.52	-163.2	-2.29	-29.98	11.3	68
0.25	-45	-4	4.44	0.4	-166.22	-1.9	-29.39	11.65	73
0.25	-45	-8	2.44	0.56	-162.59	-2.37	-29.47	11.62	76
0.25	-90	-2	7.26	0.44	-169.9	-1.7	-29.07	11.99	62
0.25	-90	-6	3.95	0.5	-169.49	-2.14	-29.32	11.67	92
0.25	135	0	11.71	0.46	-174.69	-2.04	-29.48	11.71	86
0.25	135	-4	7.03	0.49	-171.18	-2.01	**-29.01**	11.87	63
0.25	135	-8	3.61	0.45	179.69	-1.95	-29.11	11.91	78
0.25	180	-2	10.4	0.37	-170.22	-1.74	-29.11	11.69	48
0.25	180	-6	5.49	0.46	-175.14	-1.9	-29.18	11.89	62
0.25	-135	0	11.3	0.45	-176.71	-1.73	-29.31	11.88	**98**
0.25	-135	-4	6.68	0.38	167.97	-1.54	-29.42	11.82	60
0.25	-135	-8	3.49	0.5	-174.08	-2.11	-29.18	11.87	72
0.5	0	-2	3.86	0.4	173.89	-1.71	-29.1	11.97	75
0.5	0	-6	2.16	0.49	-176.69	-2.18	-29.29	11.88	73
0.5	45	0	5.28	0.44	-177.5	-1.72	-29.36	11.89	87
0.5	45	-4	3.13	0.54	-171.39	-2.32	**-29.01**	12.02	82
0.5	45	-8	1.68	0.45	-171.89	-1.99	-29.7	11.59	76
0.5	90	-2	5.62	0.42	-174.69	-1.91	-30.05	11.52	45
0.5	90	-6	3.19	0.51	-172.99	-2.3	-29.69	11.6	51
0.5	-135	0	11.31	0.41	177.71	-1.98	**-30.14**	11.46	77
0.5	-135	-4	6.28	0.44	-180	-1.66	-29.29	11.99	66
0.5	-135	-8	3.12	0.47	-165.97	-2.11	-29.65	11.42	81
0.5	135	0	11.64	0.43	-179.33	-1.69	-29.44	11.92	81
0.5	135	-4	7.09	0.47	179.27	-1.72	-29.04	11.89	57
0.5	135	-8	3.5	0.51	-170.46	-2.27	-29.04	**12.03**	76
0.5	180	-2	12.28	0.4	-179.89	-2	-29.48	11.44	45
0.5	180	-6	6.12	0.48	-167.46	-1.81	-29.04	11.82	51
Average				0.45	-173.91	-1.96	-29.40	11.71	67.17
Standard Deviation						.25	.33	.23	15.89

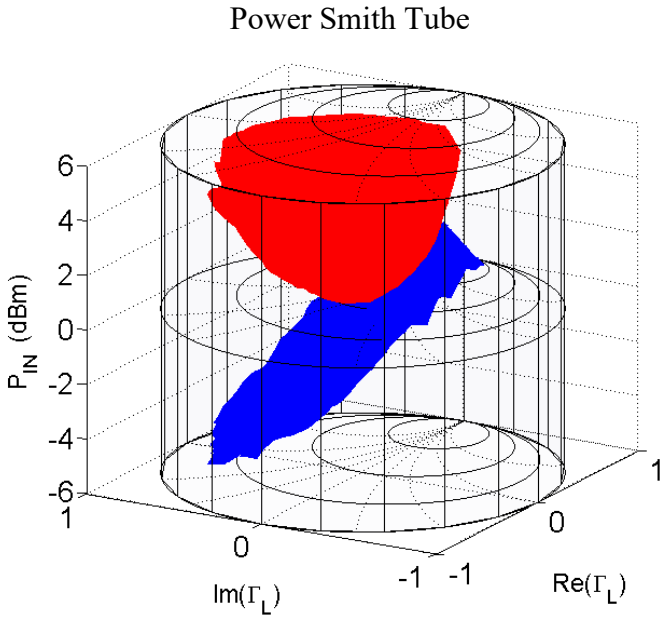

Figure 4.4. The Power Tube for the MWT-173 with a -28 dBc limit

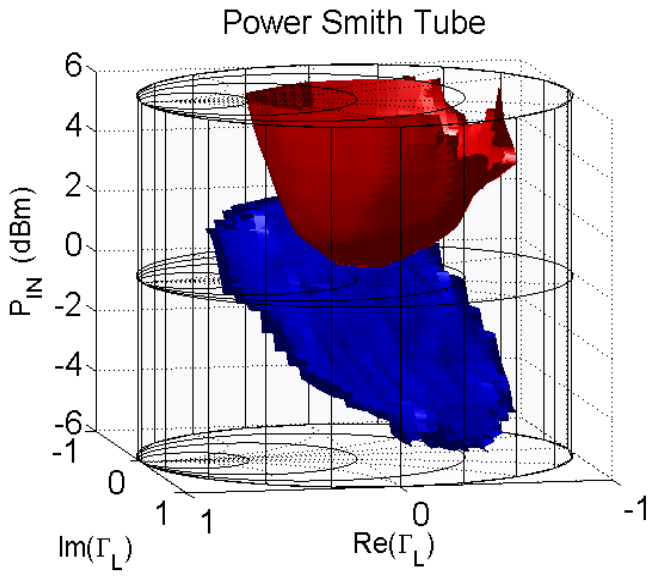

Figure 4.5. The Power Tube figure from a different angle and different lighting for the MWT-173 device

A series of searches were implemented throughout the Smith Tube from a variety of locations chosen to verify the robustness of the search. The summary of these searches is shown in Table 4.2. Figure 4.6 shows an example of a search. The search starts at

$P_{in} = 5$ dBm with Γ_L=.5/-135°. It ends at Γ_L=.31/-88.77° with $P_{in} = 1.4$ dBm in 58 measurements with PAE=24.57% and ACPR=-28.31dBc. The standard deviation of the end PAE is again relatively small which shows good convergence. The standard deviation and range of the end PAE are slightly higher than the previous case shown. This can be explained by the much larger range of PAE for this device. For this device, the PAE ranges from less than zero to almost fifty percent throughout the Power Smith Tube. The standard deviation and range of the end PAE can be reduced by decreasing the resolution distance of the search. This of course would mean that more measurements have to be taken. It was assessed that reducing the resolution distance might lead to slightly less range of end PAE, but that this was not worth doing since it also leads to more measurements.

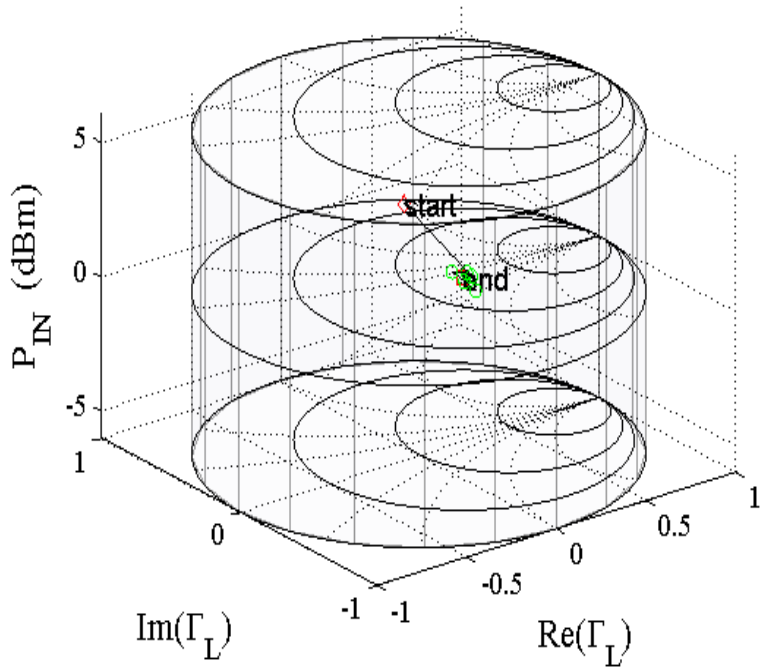

Figure 4.6. Example of a search in the Smith Tube for the MWT-173 Transistor

TABLE 4.2: SEARCH ALGORITHM RESULTS USING THE MWT-173 TRANSISTOR FOR V_{GS} = -1.5 V, $V_{DS} = 2\,V$, P_{in} = -6-6 dBm AND $ACPR_{limit} = -28\,dBc$

Start Gamma Real	Start Gamma Imag	Start Pin (dBm)	Start PAE (%)	End Gamma Mag	End Gamma Theta	End Pin (dBm)	End ACPR (dBc)	End PAE (%)	Meas
0	0	-1	21.6	0.23	-95.68	0.81	-28.48	25.3	64
0	0	-3	15.3	0.15	-59.97	0.78	-28.06	26	47
0	0	-5	8.58	0.16	-73.58	0.93	-28.43	25.32	76
0	0	1	28.54	0.25	-21.86	0.89	-28.06	25.02	43
0	0	3	35.07	0.23	-102.61	0.76	-28.26	24.77	**31**
0	0	5	39.14	0.13	-177.08	0.38	-28.16	24.94	83
0.25	0	3	31.01	0.32	-27.58	1.31	-28.01	24.99	51
0.25	0	-1	19	0.22	-111	0.55	-28.3	25.03	32
0.25	0	-5	7.48	0.13	-29.09	0.84	-28.13	26.27	50
0.25	45	1	25.84	0.19	-62.97	0.6	-28.61	25.08	42
0.25	45	5	34.21	0.19	-43.55	0.99	-28.16	26.51	64
0.25	45	-3	13.99	0.16	-80.03	1.1	-28.08	26.02	39
0.25	90	3	33.59	0.1	-54.47	0.56	-28.03	25.89	85
0.25	90	-1	20.85	0.16	-102.69	0.33	-28.36	24.63	43
0.25	90	-5	9.42	0.15	-90.7	0.42	-28.41	25.07	49
0.25	-45	1	25.4	0.15	-62.46	0.99	**-28**	26.53	47
0.25	-45	5	34.54	0.3	-87.32	1.1	-28.47	24.1	63
0.25	-45	-3	12.53	0.11	-81.09	0.19	-28.6	24.71	45
0.25	-90	3	29.97	0.12	-64.39	0.55	-28.37	25.98	81
0.25	-90	-1	18.27	0.17	-68.44	1.03	-28.05	26.65	57
0.25	-90	-5	7.26	0.23	-97.24	0.96	-28.11	26.05	91
0.25	135	1	27.12	0.24	-29.12	1.11	-28.25	24.99	61
0.25	135	5	36.62	0.32	-87.21	1.61	-28.05	24.8	49
0.25	135	-3	14.82	0.18	-124.25	0.06	-28.56	24.49	58
0.25	180	3	32.92	0.29	-75.6	1.28	-28.31	24.86	**30**
0.25	180	-1	19.9	0.23	-83.22	1.04	-28.32	25.77	70
0.25	180	-5	8.63	0.18	-46.53	1.06	-28.23	26.87	42
0.25	-135	1	23.42	0.29	-99.3	1.18	-28.07	25.23	57
0.25	-135	5	32.62	0.14	-74.56	0.69	-28.26	24.93	50
0.25	-135	-3	12.43	0.14	-40.27	0.65	-28.17	26.61	62
0.5	0	3	22.67	0.2	-21.11	0.93	-28.04	24.76	70
0.5	0	-1	14.02	0.04	-109.86	0.01	-28.25	25.35	50
0.5	0	-5	5.74	0.12	-125.68	0.02	-28.56	24.84	49
0.5	45	1	19.56	0.12	-91.45	0.53	-28.25	24.87	50
0.5	45	5	26.65	0.26	-32.75	0.94	-28.29	24.58	66
0.5	45	-3	10.76	0.26	-105.16	0.74	-28.25	24.7	60
0.5	90	3	26	0.15	-35.53	0.31	-28.64	24.46	43
0.5	90	-1	15.74	0.18	-95.78	0.81	-28.09	26.13	82
0.5	90	-5	7.25	0.11	-53.34	0.28	-28.69	25.51	54
0.5	-135	1	20.69	0.07	-111.37	-0.21	-28.47	24.13	63
0.5	-135	5	30.5	0.31	-88.77	1.4	-28.31	24.57	58
0.5	-135	-3	10.94	0.18	-70.89	0.96	-28.06	26.24	72
0.5	-90	3	22.57	0.14	-68.69	0.79	-28.04	26.73	68
0.5	-90	-1	13.42	0.22	-81.66	0.91	-28.43	25.24	51
0.5	-90	-5	5.35	0.09	-39.28	0.81	-28.02	**27.24**	**101**
0.5	135	1	21.31	0.16	-61.45	0.8	-28.03	25.7	69
0.5	135	5	32.03	0.17	-87.79	0.68	-28.14	24.81	58
0.5	135	-3	11.64	0.14	-39.21	0.68	-28.2	26.83	50
0.5	180	3	26.31	0.26	-106.21	0.88	-28.05	24.99	52
0.5	180	-1	16.51	0.1	-117.78	0.21	-28.17	25.26	51
0.5	180	-5	7.48	0.14	-120.62	-0.13	**-28.68**	**24**	47
		Averages	20.53	0.18	-74.12	0.73	-28.26	25.38	57.37
		Standard Deviation					.2	.80	15.3

In this chapter, optimization in the Power Smith Tube was demonstrated using a varactor matching network as a tuner. The power-dependent algorithm presented in the previous chapter was expanded and implemented in the Power Smith Tube. This successfully demonstrates a multi-variable optimization using a varactor tuner.

CHAPTER FIVE

Circuit Optimization Using Resonant Cavity Tuner Position Number

Optimization was also sought with the resonant cavity tuner because of its ability to handle high input power, which is vital in radar use, and its high bandwidth. The evanescent mode resonant cavity tuner presented many challenges that the varactor tuner did not present. While the resonant cavity tuner does not experience significant non-linearity in its typical range of operation, repeatability can be an issue in load optimization measurements. It was discovered that the tuner would lose its characterization over time. Sensitivity to movement and temperature changes was also observed. Figure 5.1 shows measurements performed by Baylor student Chris Kappelmann that exemplifies the changes in the S-parameters of the tuner. The measurements show the average error in the S-parameters of all points in a characterization over a period of 60 hours. A steady drift is observed over time, and the S-parameters change significantly at around the 55th hour when the air conditioning was turned on in the environment. Some of these issues can be attributed to the extremely small gap space of the cavities which is on the order of micrometers. The tuner would also occasionally experience a failure in its control loop, causing it to go to a value of load reflection coefficient Γ_L far from the intended location on the Smith Chart. For all these reasons, it was decided that using fundamental tuning elements as the search space could be very useful. Using the fundamental elements, in this case resonant cavity position number (n), would prevent the need for any characterization mapping Γ_L to

(n_1, n_2) combinations. This approach eliminates the need for characterization look-up tables, and the time required to perform a characterization can be eliminated. Typically, at least an hour is needed for a useable characterization, and the characterization should be repeated every several hours due to potential drift. As such, direct tuning using the resonant cavity position numbers is expected to result in significant time savings.

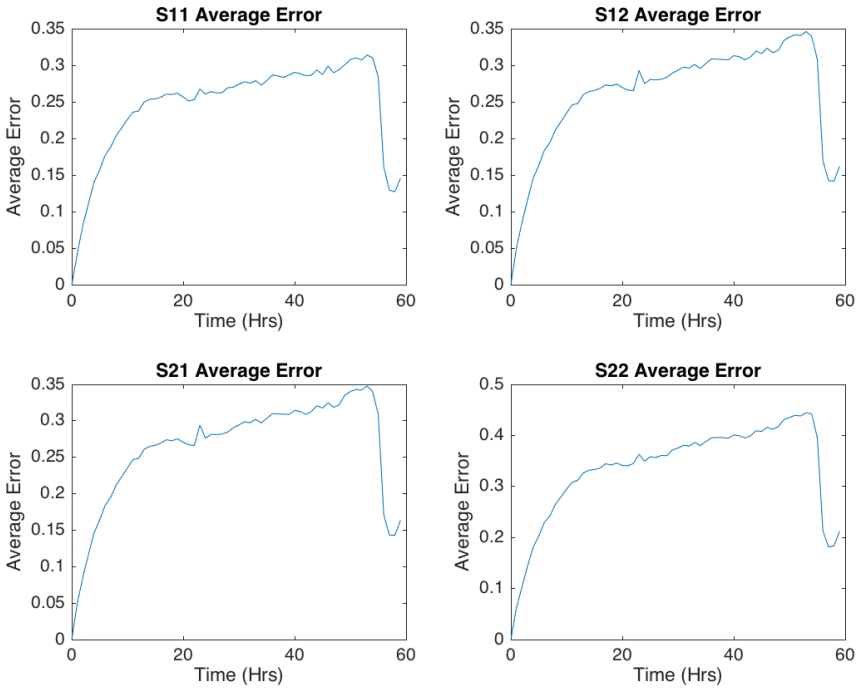

Figure 5.1. S-parmeters of tuner over 60 hours

One of the issues that quickly became apparent when load-pull measurements were taken was that this search space possessed some undesirable optimization characteristic. Contours show that ACPR is multimodal meaning that there was a local minimum separate from the global one. This is most likely due to the fact that different combinations of n_1 and n_2 often map to the same Γ_L. Figure 5.5 and 5.6 shows examples of typical contours generated from varying n_1 and n_2 in increments across the search

space at 3.3 GHz. Even though the PAE contours do not appear multimodal, it was still discovered that the gradient search had issues converging for a PAE only search when starting at locations very far away from the optimum. This is due to the shallowness or flatness of the contours in these regions which falsely guide the algorithm into believing it has reached an optimum.

A simple plan was devised to attempt to solve this problem. The reason the algorithm encountered issues was because it did not start close to the optimum. Instead, it either started so far away that the contours were very shallow, or it would start at a location where it would end up in the local minimum. Therefore, instead of testing the algorithm from anywhere, it is good idea to have the algorithm try to choose a smart start location. This can be achieved by having the algorithm test some points that are spread around the search space and starting from the best one. This can potentially lead to a point with very low-efficiency being measured which can damage some high-powered amplifiers. However, this is an issue that would also be encountered if the search was started and tested from any random location which was how the algorithm was implemented previously.

It was initially decided to test the algorithm with PAE optimization only since it previously had issues converging even with a PAE-only search. Since the S_{21} of the tuner is not measured when tuning with the fundamental elements only, the output of the tuner is used as the reference plane for the measurements. The PAE shown in this section is the efficiency of the DUT and tuner together, and therefore it is considerably less than the device alone since there is loss in the tuner. The device tested is the Skyworks packaged amplifier biased to 7 V. The input power is 3 dBm. The operating frequency is 3.3 GHz

which is the design frequency of the tuner. Figure 5.2 shows the resonant cavity position load-pull. Table 5.1 shows results taken from a PAE-only search from various starting points around the search space. There are several starting points that fail to converge to the correct optimum. This illustrates how even the PAE only search encounters issues when started from any locations.

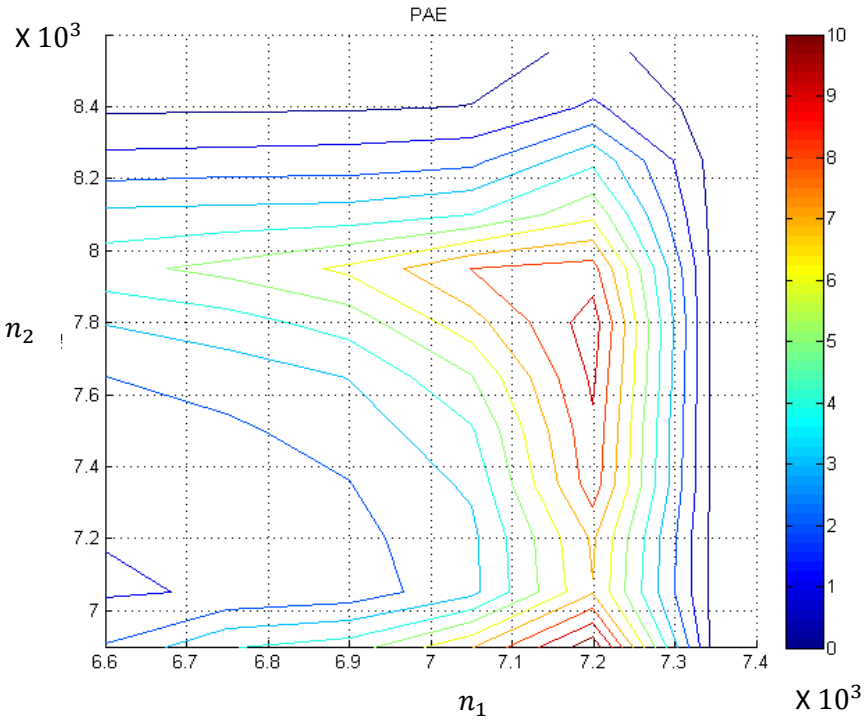

Figure 5.2. Resonant cavity position load-pull at 3.3 GHz for the Skyworks amplifier

The five starting locations are illustrated in Figure 5.3. The locations of the four points in the corners are obtained by dividing the search space range in n_1 and n_2 by one-third and creating a matrix of start locations based on the combination of these values. The point in the middle is exactly in the middle of the search space. The five points are measured and the one with the highest PAE is chosen as the start location of the search. To test accuracy, the algorithm was implemented ten times. Table 5.2 shows

these results. Figure 5.4 shows an example of a typical search. As expected, the algorithm always starts at the top right point which is very close to the optimum. The algorithm converges extremely well. Table 5.3 shows a comparison of the modified search with the original. The search has improved in all areas, even in number of measurements, despite having to take five extra measurements in the beginning of the search. This is reassuring moving onto the constrained search.

Table 5.1. Summary of searches with the gradient algorithm at 3.3 GHz for the Skyworks amplifier

Start n_1	Start n_2	Start PAE (%)	End n_1	End n_2	End PAE (%)	Total Measurements
6975	7600	3.75	7171	7690	11.30	16
6975	7600	3.44	7184	7704	11.19	19
7225	8067	5.61	7152	7842	11.41	25
6725	8067	3.80	7150	7845	11.40	37
7225	7133	2.71	7187	7315	9.66	22
6725	7600	2.39	7171	7843	11.26	20
7225	7600	4.91	7156	7785	11.55	22
6975	8067	4.00	7182	7811	11.38	22
6975	7133	1.79	7202	7253	9.56	13
6725	7133	1.17	7183	7505	10.46	31
Average		3.36	7173.78	7659.23	10.92	22.7
Standard Deviation			17.13	223.73	0.75	6.99

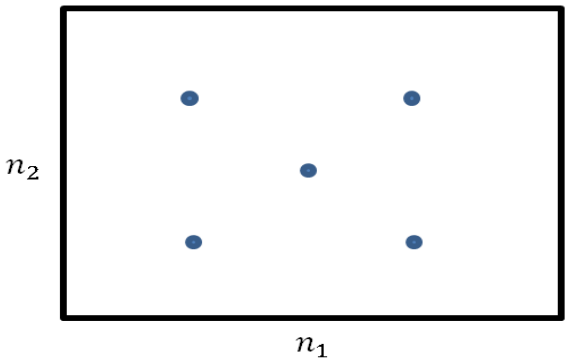

Figure 5.3. The tested start locations for the modified resonant frequency search

Table 5.2. Summary of searches with the modified gradient algorithm at 3.3 GHz for the Skyworks amplifier

Start n_1	Start n_2	Start PAE (%)	End n_1	End n_2	End PAE (%)	Total Measurements
7100	7833	10.28	7150	7833	11.40	15
7100	7833	10.37	7133	7813	11.39	18
7100	7833	10.38	7132	7804	11.38	18
7100	7833	10.42	7130	7796	11.38	18
7100	7833	10.46	7142	7785	11.55	21
7100	7833	10.55	7138	7772	11.58	18
7100	7833	10.54	7137	7771	11.56	18
7100	7833	10.57	7135	7766	11.55	18
7100	7833	10.57	7135	7766	11.55	18
7100	7833	10.64	7153	7767	11.59	18
Average		10.48	7138.37	7787.25	11.49	18
Standard Deviation			7.67	23.46	0.09	1.41

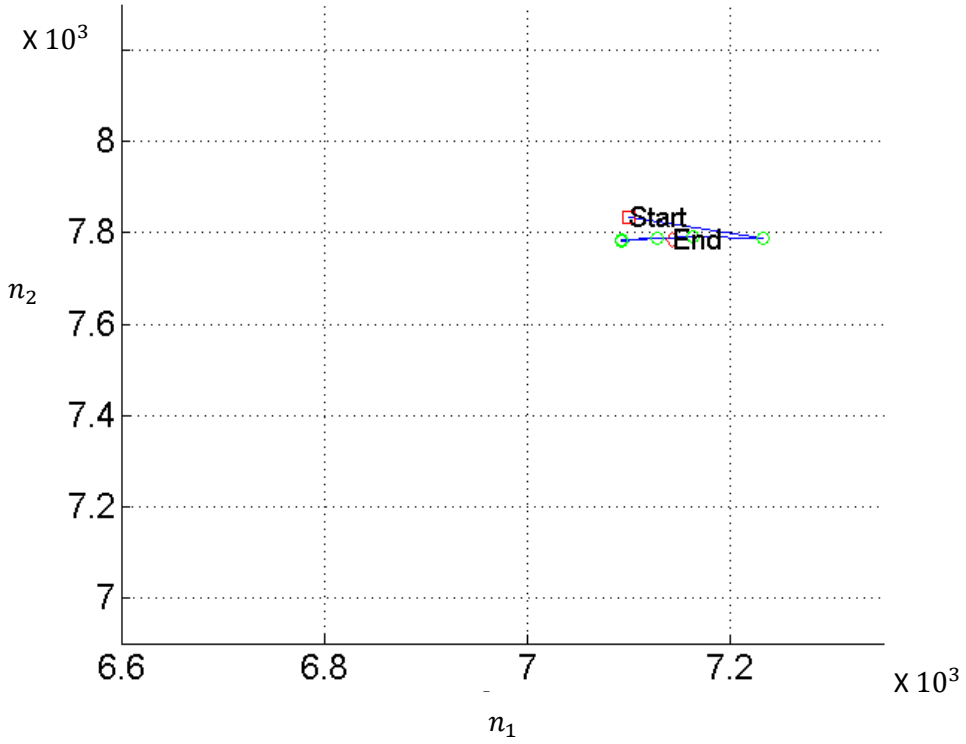

Figure 5.4. Example of a typical search trajectory of the modified gradient search at 3.3 GHz for the Skyworks amplifier

Table 5.3. Comparison of the gradient search to the modified search at 3.3 GHz

	Gradient Search	Modified Gradient Search
PAE Average (%)	10.92	11.49
PAE Standard Deviation	0.75	0.09
Average Num of Measurements	22.7	18
Std Dev of Num of Measurement	6.99	1.41
Average End n	7137.78, 7659.23	7138.37, 7787.25

Choosing a suitable start point when using a constraint search was more of a challenge. Simply choosing the test point with the highest PAE will not always start the search in the location closest to the optimum. A scale was developed that weights both PAE and ACPR to try and come up with the most suitable start location. This scale tries to normalize both PAE and ACPR so that they both play equal parts in determining the best test point. This is given in equation 5.1 where PAE_{cand} is the PAE at the candidate start location, PAE_{max} is the highest PAE measured among the locations tested, $ACPR_{cand}$ is the measured ACPR at the candidate start location, and $ACPR_{lim}$ is the ACPR limit. The test start location with the lowest scale number is chosen as the most suitable start location.

$$Start_{best} = \left|\frac{PAE_{cand} - PAE_{max}}{PAE_{max}}\right| + \left|\frac{ACPR_{cand} - ACPR_{lim}}{ACPR_{lim}}\right| \qquad (5.1)$$

The Skyworks device was tested again, but now also with an ACPR constraint. Figure 5.5 and 5.6 show the (n_1, n_2) load-pull. -25 dBc was chosen as the limit. Although this is a very strict limit, it provides an adequate constraint on the PAE so that it does not simply converge to its maximum value. According to the full load-pull measurement, the point with best PAE with ACPR Constraint is located at n_1 =7200 and n_2 =7400 with PAE of 9.12% and ACPR of -25.24 dBc. The search was implemented ten times. Results

are shown in Table 5.4. It always starts on the bottom right corner. It converges well as evidenced by the low standard deviation of the end PAE. ACPR does have some noise that contributes to the algorithm not being as extremely repeatable as when it was a PAE search only.

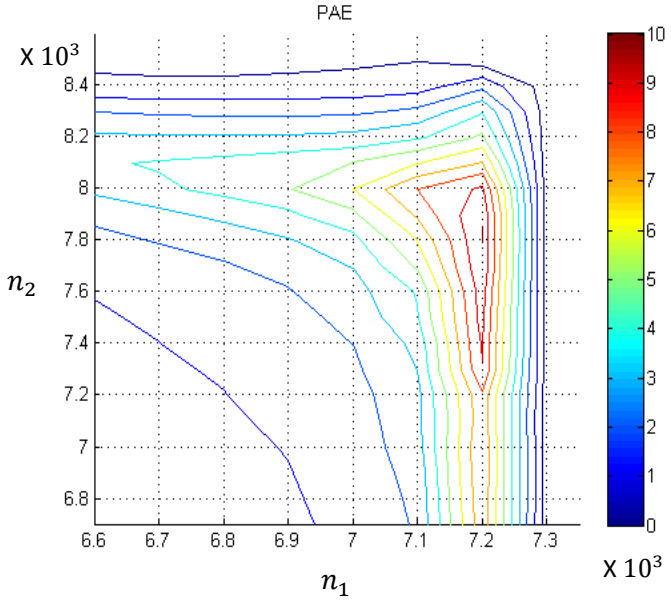

Figure 5.5. PAE load-pull measurement at 3.3 GHz for the Skyworks Amplifier

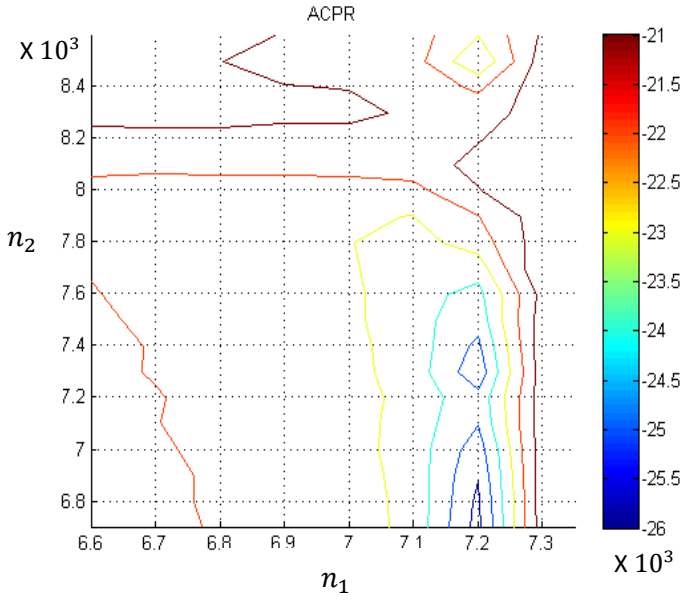

Figure 5.6. ACPR load-pull measurement at 3.3 GHz for the Skyworks Amplifier

Table 5.4. Summary of search algorithm at 3.3 GHz with an ACPR constraint of -25 dBc using the Skyworks amplifier

Start n_1	Start n_2	Start PAE (%)	Start ACPR (dBc)	End n_1	End n_2	End PAE (%)	End ACPR (dBc)	Total Measurements
7100	7333	3.36	-23.47	7188	7339	9.01	-25.50	31
7100	7333	3.39	-23.49	7190	7341	9.16	-25.50	25
7100	7333	3.44	-23.47	7187	7383	9.27	-25.40	61
7100	7333	3.45	-23.51	7189	7340	9.18	-25.66	31
7100	7333	3.46	-23.53	7188	7341	9.14	-25.54	25
7100	7333	3.46	-23.51	7188	7331	9.10	-25.56	25
7100	7333	3.45	-23.50	7188	7336	9.11	-25.48	31
7100	7333	3.47	-23.55	7187	7334	9.06	-25.33	46
7100	7333	3.44	-23.54	7187	7330	9.02	-25.43	37
7100	7333	3.44	-23.49	7188	7338	9.12	-25.35	25
Average		3.44	-23.51	7188	7341.3	9.12	-25.47	33.7
Standard Deviation				0.94	15.17	0.08	0.1	11.7

The modified algorithm was also tested on another device to confirm its performance. The MWT-173 transistor was biased to a drain voltage of 4 V and a gate voltage of -1.5 V. The input power was set to 14 dBm which about three dB into compression. The resonant position load-pulls are shown in figure 5.7 and 5.8. The limit was chosen to be -28 dBc. According to the load pull, the point with best PAE with ACPR the constrained optimum is located at n_1=7200 and n_2 =7400 with PAE of 7.22 and ACPR of -28.09 dBc. The results from the searches are shown in Table 5.5. The search again converges proving that the search is robust and can work on multiple devices. Figure 5.9 shows an example of a typical search.

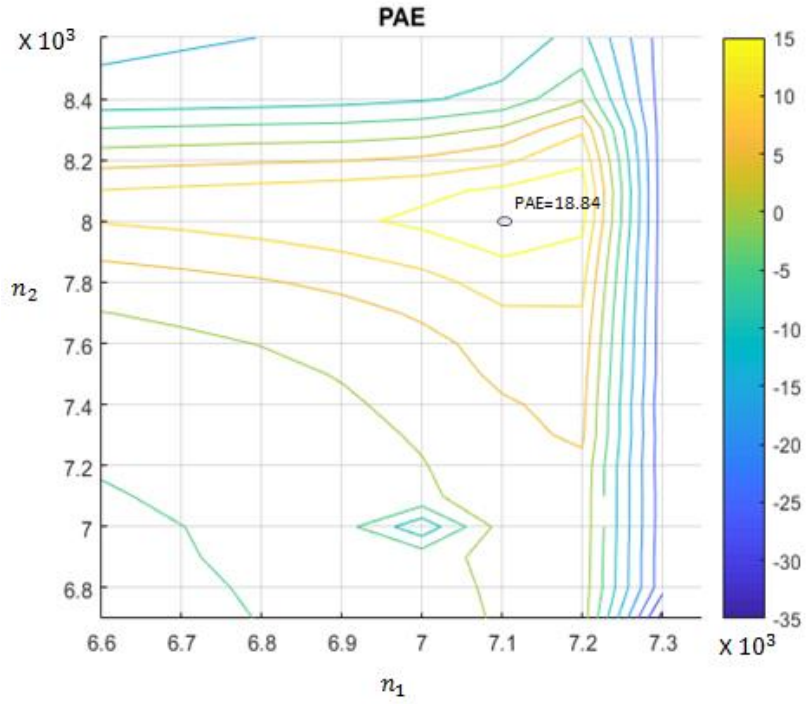

Figure 5.7. PAE load pull at 3.3 GHz with an input power of 14 dBm with the MWT-173 FET

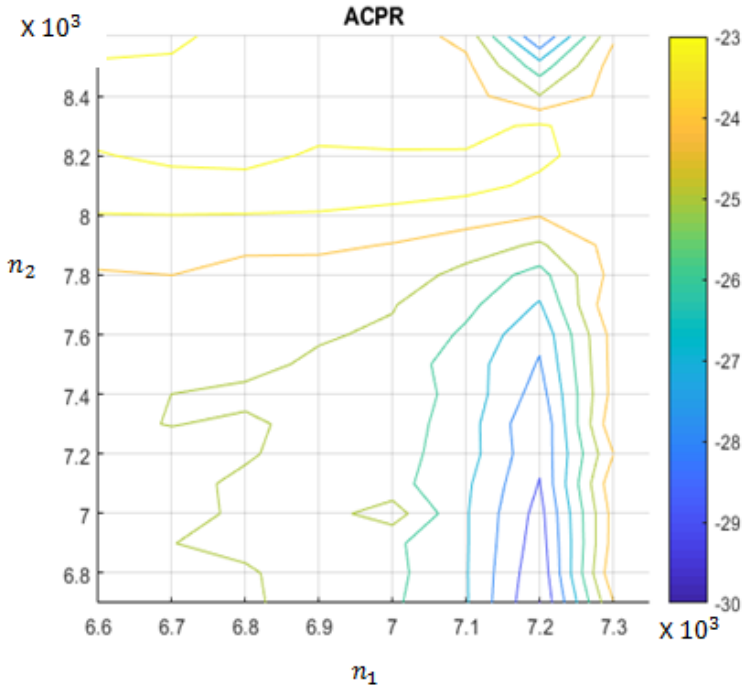

Figure 5.8. ACPR load pull at 3.3 GHz with an input power of 14 dBm with the MWT-173 FET

Table 5.5. Summary of search algorithm at 3.3 GHz with an ACPR constraint of -28 dBc using the MWT-173 FET

Start n_1	Start n_2	Start PAE (%)	Start ACPR (dBc)	End n_1	End n_2	End PAE (%)	End ACPR (dBc)	Total Measurements
7100	7333	3.86	-25.02	7179	7445	7.63	-28.24	13
7100	7333	3.82	-26.23	7176	7454	7.86	-28.08	16
7100	7333	3.75	-26.24	7176	7440	7.70	-28.15	25
7100	7333	3.75	-26.19	7171	7419	7.37	-28.19	25
7100	7333	3.69	-26.28	7177	7408	7.35	-28.23	25
7100	7333	3.70	-26.31	7173	7433	7.51	-28.08	25
7100	7333	3.68	-26.18	7187	7452	7.87	-28.21	22
7100	7333	3.67	-26.13	7188	7451	7.87	-28.23	28
7100	7333	3.65	-26.13	7188	7456	7.92	-28.18	25
7100	7333	3.80	-26.14	7189	7450	7.91	-28.35	22
Average		3.74	-26.08	7180.4	7440.8	7.70	-28.19	22.6
Standard Deviation				6.9	16.16	0.22	0.08	4.65

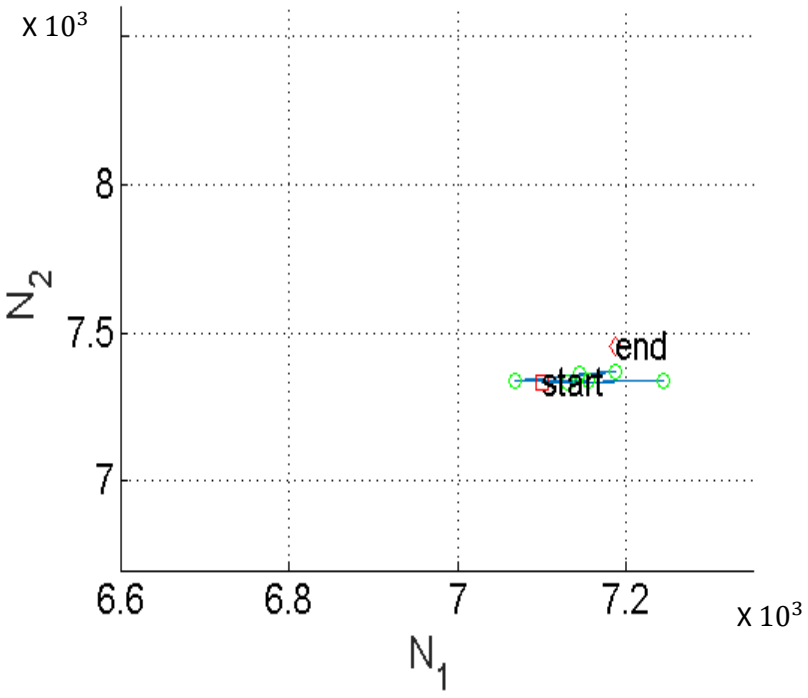

Figure 5.9. Example of a typical search with a -28 dBc limit for the MWT-173 FET. The search converges to $n_1 = 7188$ and $n_2 = 7456$ with a PAE of 7.92 % and an ACPR of -28.18

In conclusion, circuit optimization using the resonant cavity position numbers of an evanescent mode resonant cavity tuner was demonstrated. There were some challenges that were encountered in this search space, but they were mitigated by attempting to have the search choose a smart start location to start from. Eliminating the use of a characterization saves time and avoids the non-ideal issues associated with characterizing this tuner. The use of this tuner takes us closer to implementing real-time optimization on devices that can be used in a radar.

CHAPTER SIX

Frequency Agility Using a Resonant Cavity Tuner

This chapter has been accepted for publication as [3] S. Rezayat, C. Kappelmann, Z. Hays, C. Baylis, D. Peroulis, A. Semnani, and E. Viverios. "Real-Time Frequency-Agile Circuit Optimization for S-Band Radar Using a High-Power Tunable Resonant Cavity Matching Network," *IEEE MTT-S International Microwave Symposium*, June 2018.

As mentioned in the background, future radar systems will need to be able to change operating frequency and bandwidth depending on surrounding devices. The resonant cavity tuner has a bandwidth of approximately 30%. The tuner can operate from 3.1 to 3.5 GHz. This covers 42% of the S-band radar allocation which starts at approximately 3.1 GHz and end at the 4 GHz which is the upper frequency limit of the S-band. Therefore, reconfiguring frequency and spectral requirements should be verified using the algorithms described with tunable circuitry. The algorithm will have to constantly optimize as its frequency changes. This concept of changing frequency when optimizing is called "frequency agility".

When approaching the idea of implementing frequency agility, it was initially decided that the search should be implemented on the Smith Chart. The Smith Chart provides a more easily navigated search space in terms of the shapes of its contours representing PAE and ACPR. However, it was also decided that the resonant cavity search should also be implemented in the resonant cavity position number (n_1, n_2) plane in order to take advantage of the benefits of both search spaces. The search initially starts in the Smith Chart, since the algorithm typically can converge from anywhere on the Smith Chart, and then it proceeds to search the resonant cavity position space, since the

search can reach finer resolutions in this search domain. When there is a frequency shift, the search will start where the previous search left off on the Smith Chart.

For the searches implemented in this section, the algorithm was slightly modified. Three neighboring points were used to calculate the gradient instead of two in both search spaces. This gives more accurate results for the gradient. It is especially useful when searching with a characterization where the density of the characterization might limit the number of points that can be precisely reached. It is also useful in the (n_1, n_2) plane where there are non-convexities that prevent the algorithm from calculating the gradient correctly. Figure 6.1(a) shows the three neighboring points that are used to calculate the gradient, and Figure 6.1(b) and Figure 6.1(c) show the construction of the search vector in the cases of initial non-compliance and compliance, respectively.

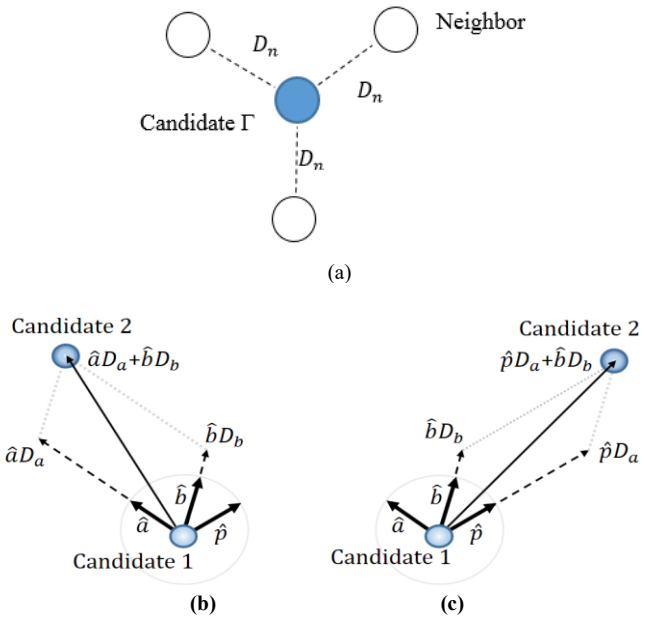

Figure 6.1. (a) Measurements for estimation of the gradient and calculation of the search vector to the next candidate when (b) the ACPR at candidate 1 is greater than the ACPR constraint (out of compliance), and (c) the ACPR at candidate 1 is less than or equal to the ACPR constraint (in compliance)

To compare with the results of the reconfiguration searches, full load-pull measurements were performed on the Smith Chart and the (n_1, n_2) plane at 3.1, 3.3, and 3.5 GHz. For these measurements, a Microwave Technologies MWT-173 transistor was used biased at V_{GS} = -1.5 V, $V_{DS} = 4\,V$, and $P_{in} = 14\,dBm$. Figure 6.2 shows the load-pull measurement results at 3.1 GHz, Figure 6.3 shows the load-pull measurement results at 3.3 GHz, and Figure 6.4 shows the load-pulls at 3.5 GHz. The figures also point out the constrained optimum for the limits chosen for the search. Figure 6.2 shows some disparities between the (n_1, n_2) load-pull and the Smith Chart one. The PAE optimum is not consistent between the two figures and the (n_1, n_2) load-pull does not seem to have any ACPR unacceptable region. This is because the resolutions of these load-pulls are different. At 3.1 GHz, tuning across the Smith Chart can take place in a small region near the PAE optimum in the (n_1, n_2) plane. When a characterization is taken, there is higher density of points taken in this region, but during (n_1, n_2) load-pull the points are evenly distributed.

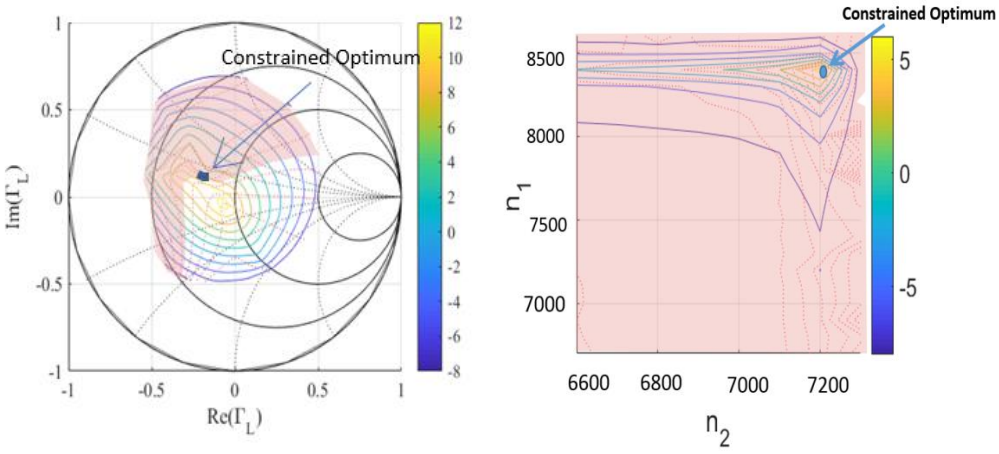

Figure 6.2. Amplifier load-pull on the Smith Chart (left) and resonant cavity position space (right) at 3.1 GHz with a -33 dBc ACPR limit shown.

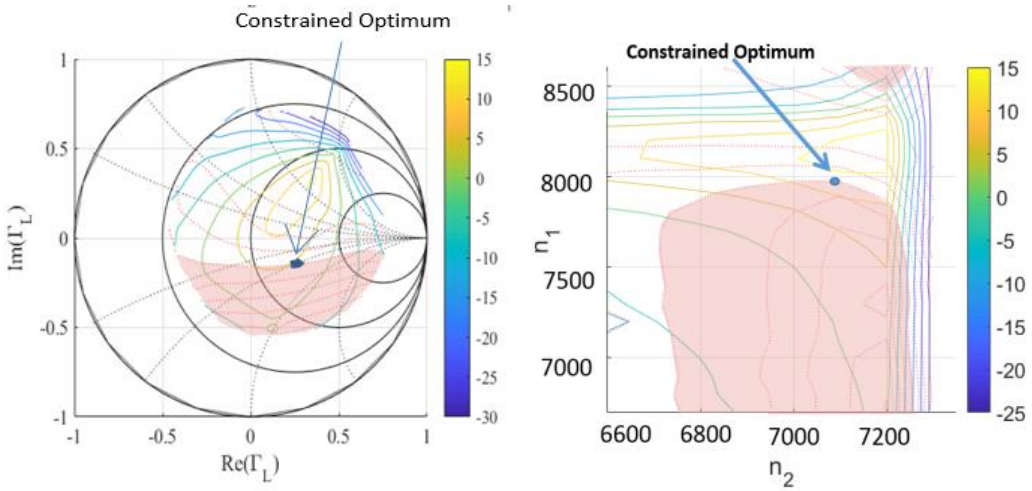

Figure 6.3. Amplifier load-pull on the Smith chart (left) and resonant cavity position space (right) at 3.3 GHz with a -31 dBc ACPR limit shown.

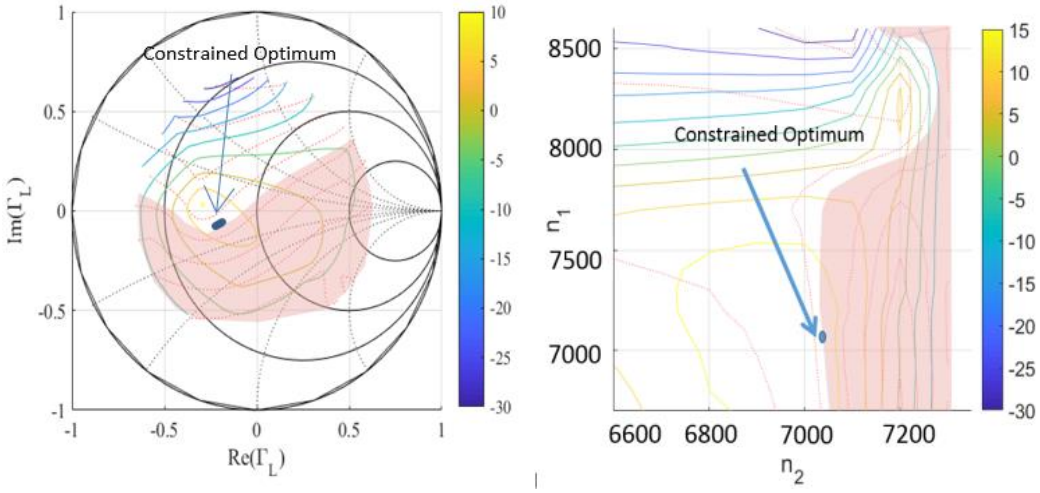

Figure 6.4. Amplifier load-pull on the Smith chart (left) and the resonant cavity position space (right) at 3.5 GHz with a -30 dBc ACPR limit shown.

A series of searches at the different frequencies was implemented. The search started at 3.1 GHz with a -33 dBc limit. Table 6.1 shows all the steps of the search. The search approaches the optimum on the Smith Chart. After candidate seven, the search switches to the (n_1, n_2) plane where it takes a couple of steps that slightly improve the PAE. The search trajectory of the search on the Smith Chart and (n_1, n_2) plane is shown

in Figure 6.5. The device is then switched to 3.5 GHz with a limit of -31 dBc. The device starts at the closest point it can find to where it left at 3.1 GHz on the Smith Chart. This will correspond to a different (n_1, n_2) combination than the previous frequency since a different characterization is used at each frequency. This time, there are more steps taken on the (n_1, n_2) plane, but the search substantially improves in this domain. Figure 6. 6 illustrates the search trajectory. Lastly, the search moves to the 3.3 GHz with a -30 dBc limit. It starts out of the ACPR-compliant region but is able to reach it in its Smith Chart search. It does not improve substantially in the resonant cavity search. Figure 6.7 illustrates this search. The average time per measurement for results is 6.7 seconds. This is mostly due to the settling time of the tuner. There is also some equipment over-head. The next generation of the setup will aim to reduce time per measurement by using a tuner that takes much shorter time to settle.

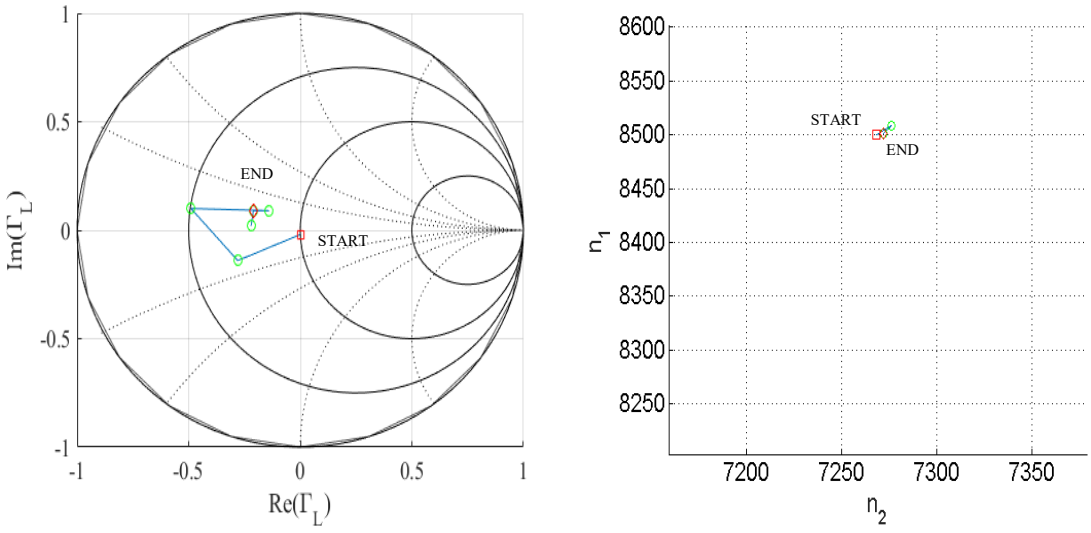

Figure 6.5. Search trajectory on the Smith chart (left) and resonant cavity position space (left) at 3.1 GHz with a -33 dBc ACPR limit.

TABLE 6.1. SUMMARY OF FREQUENCY AGILITY SEARCH

Freq. (GHz)	ACPR Limit (dBC)	Cand	Γ_L	n_1	n_2	PAE (%)	ACPR (dBc)	Total Meas.
3.1	-33	1	0.02 ∠-90	7238	8300	16.29	-28.62	1
3.1	-33	2	0.313 ∠168.47	7252	8300	11.89	-28.75	5
3.1	-33	3	0.50 ∠168.46	7266	8400	1.75	-36.95	9
3.1	-33	4	0.17 ∠147.27	7238	8350	7.72	-35.33	14
3.1	-33	5	0.23 ∠156.80	7268	8500	10.83	-34.88	18
3.1	-33	6	0.22 ∠174.81	7246	8350	12.71	-30.84	22
3.1	-33	7	0.22 ∠156.80	7268	8500	10.84	-34.87	25
3.1	-33	8	(n_1, n_2) Search	7276	8508	4.15	-34.74	29
3.1	-33	9	(n_1, n_2) Search	7272	8501	11.34	-33.54	31
3.5	-31	10	0.24 ∠155.56	7230	8150	11	-28.69	32
3.5	-31	11	0.41 ∠-88.60	7198	6800	-1	-35.91	36
3.5	-31	12	0.44 ∠-128.66	7220	7450	-2.01	-34.48	40
3.5	-31	13	0.40 ∠-112.07	7212	7300	-0.68	-34.78	41
3.5	-31	14	0.35 ∠-85.10	7186	7100	0.82	-35.07	45
3.5	-31	15	0.32 ∠-57.80	7175	7000	2.9	-34.77	49
3.5	-31	16	0.23 ∠-74.75	7175	7500	5.24	-32.75	53
3.5	-31	17	0.11 ∠-56.31	7150	7650	8.17	-30.97	57
3.5	-31	18	0.23 ∠-74.75	7175	7500	5.26	-32.76	58
3.5	-31	19	(n_1, n_2) Search	7161	7498	7.02	-32.21	62
3.5	-31	20	(n_1, n_2) Search	7151	7498	8.05	-31.81	66
3.5	-31	21	(n_1, n_2) Search	7144	7498	8.7	-31.6	70
3.5	-31	22	(n_1, n_2) Search	7139	7497	9.18	-31.4	74
3.5	-31	23	(n_1, n_2) Search	7136	7496	9.42	-31.25	78
3.3	-30	24	0.21 ∠-79.22	7198	8040	16.06	-26.27	79
3.3	-30	25	0.47 ∠-113.35	7248	8600	-6.32	-35.35	83
3.3	-30	26	0.45 ∠-137.73	7246	8500	3.86	-34.79	87
3.3	-30	27	0.48 ∠-40.73	7236	8600	-5.54	-32.8	91
3.3	-30	28	0.41 ∠-32.15	7175	7800	10.56	-32.8	92
3.3	-30	29	0.37 ∠-3.09	7150	8010	12.27	-28.29	96
3.3	-30	30	0.41 ∠-32.15	7175	7800	10.56	-32.68	97
3.3	-30	31	(n_1, n_2) Search	7124	7805	9.23	-33.3	101
3.3	-30	32	(n_1, n_2) Search	7149	7802	10.15	-33.31	102
3.3	-30	33	(n_1, n_2) Search	7172	7800	10.57	-32.82	105

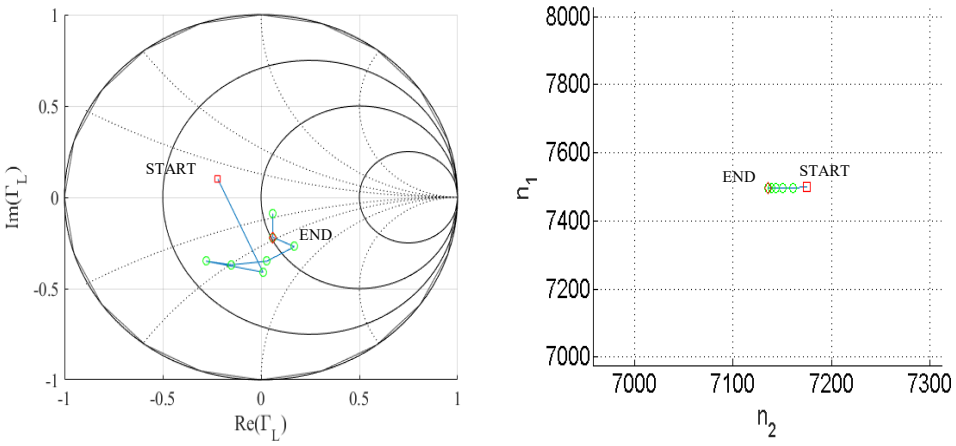

Figure 6.6. Search trajectory on the Smith chart (left) and resonant cavity position space (left) at 3.5 GHz with a -31 dBc ACPR limit.

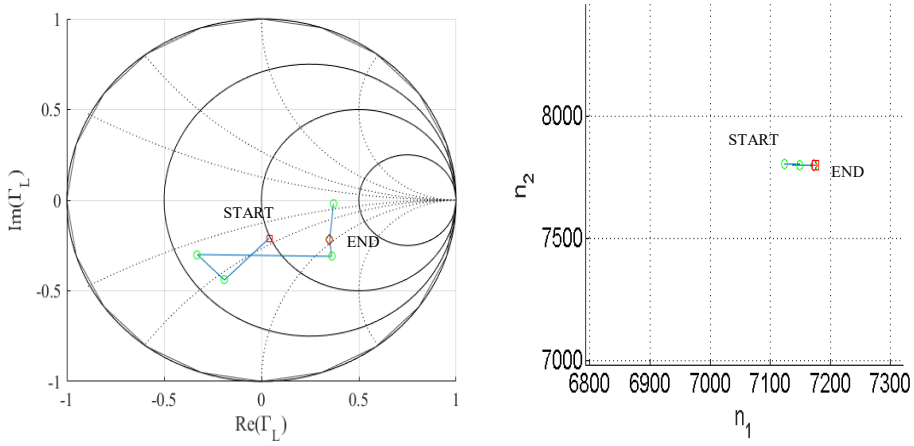

Figure 6.7. Search trajectory on the Smith chart (left) and resonant cavity position space (left) at 3.3 GHz with a -30 dBc ACPR limit.

Optimization of a high-power handling resonant cavity tuner under different ACPR constraint has been demonstrated. When operating frequencies are changed, the search uses a modified gradient search on the Smith Chart to initially optimize. The search is then switched to the resonant cavity position number space to avoid characterization drift and non-idealities. The demonstration of intelligent reconfigurability using a high-power tunable matching network is a significant step toward the design of adaptive transmitters for cognitive or adaptive radar.

CHAPTER SEVEN

Conclusions

This thesis has presented algorithms for a cognitive radar that can continuously adapt to the requirements placed upon it. More specifically, this thesis has presented multiple techniques for optimizing the circuitry for a cognitive radar using two different types of impedance tuners that are more suited to work with radar. The concept of continuous circuit optimization while performing frequency agility was also introduced and demonstrated.

The first tuner that was used for these optimizations was a varactor tuner. This tuner required the development of an algorithm to mitigate the non-linearity that it possessed. The solution to this was presented as the power-dependent characterization which was proven to improve measurements and circuit optimization.

An evanescent-mode resonant cavity tuner was also used to implement the optimization algorithm. This impedance tuner can handle high power levels and has a large bandwidth. The fundamental tuning elements of the tuner were used for optimization to take advantage of the simplicity offered with this approach. The search space in this domain often contains non-convexities and multimodalities, so the search had to be modified to have the searches run successfully. Results demonstrated successful constraint optimization using the fundamental elements of the resonant cavity tuner.

The last concept that was explored is frequency agility where the operating frequency of the circuit is shifted, but the circuit is still continuously optimized. This was

ideal to test with the resonant cavity tuner since it has a large bandwidth. A hybrid approach was chosen to be implemented, where the search was implemented initially on the Smith Chart and then completed in the resonant cavity position number space. This search provides robustness to the algorithm. Frequency agility was successfully demonstrated over a significant part of the S-band which has been the targeted for spectrum sharing. Multiple concepts have been presented in this thesis that will be needed to implement transmitter circuitry for a cognitive or adaptive radar. Future work should include the use of a software defined radio that simulates an intelligent radar, choosing its operating frequency and bandwidth based on constraints from systems around it. This setup should be incorporated with circuit and waveform optimization using the resonant cavity tuner.

REFERENCES

[1] *National Broadband Plan*, http://www.broadband.gov

[2] S. Haykin, "Cognitive Radar: A Way of the Future*," IEEE Signal Processing Magazine*, January 2006, pp. 30-40.

[3] J. Guerci, Cognitive Radar: The Knowledge-Aided FullyAdaptive Approach, Artech House, 2010

[4] S. Rezayat, C. Kappelmann, Z. Hays, L. Lamers, C. Baylis, E. Viveiros, A. Hedden, J. Penn, and R. Marks II. "Real-Time Amplifier Load-Impedance Optimization for Adaptive Radar Transmitters Using a Nonlinear Tunable Varactor Matching Network," *IEEE Transactions on Aerospace and Electronic Systems,* 2017.

[5] S. Rezayat, C. Kappelmann, Z. Hays, C. Baylis, D. Peroulis, A. Semnani, and E. Viverios. "Real-Time Frequency-Agile Circuit Optimization for S-Band Radar Using a High-Power Tunable Resonant Cavity Matching Network," *IEEE MTT-S International Microwave Symposium*, June 2018.

[6] L.E. Brennan, I.S. Reed, "Theory of Adaptive Radar," *IEEE Transactions on Aerospace and Electronic Systems*, Vol. 9, No.2, March 1973, pp. 237-252.

[7] J.S. Goldstein and I.S. Reed, "Theory of Partially Adaptive Radar," *IEEE Transactions on Aerospace and Electronic Systems*, Vol. 33, No. 4, October 1997, pp. 1309-1325.

[8] V. Ramaswamy and J.T. Correia, "Enabling Spectrum Sharing between LTE and RADAR Systems in S-band," *2017 IEEE Wireless Communications and Networking Conference*, San Francisco, California, March 2017.

[9] A.F. Martone, K.D. Sherbondy, K.I. Ranney, T.V. Dogaru, "Passive sensing for adaptable radar bandwidth," in Proc. of the *2015 IEEE Radar Conference*, Arlington,Va, May 2015, pp. 0280 – 0285.

[10] A. Martone, C. Dietlein, M. Govoni, K. Sherbondy and J. Pulskamp, "Tuning Technology for Adaptable Radar Bandwidth," *2016 IEEE MTT-S International Microwave Symposium (IMS),* San Francisco, CA, 2016.

[11] L.K. Patton and B.D. Rigling, "Autocorrelation Constraints in Radar Waveform Optimization for Detection," *IEEE Transactions on Aerospace and Electronic Systems*, Vol. 48, No. 2, April 2012, pp. 951-968.

[12] L.K. Patton and B.D. Rigling, “Phase Retrieval for Radar Waveform Optimization,” *IEEE Transactions on Aerospace and Electronic Systems*, Vol. 48, No. 4, October 2012., pp.3287-3302.

[13] L.K. Patton and B.D. Rigling, “Autocorrelation and Modulus Constraints in Radar Waveform Optimization,” 2009 International Waveform Diversity and Design.

[14] L. Ryan, J. Jakabosky, S.D. Blunt, C. Allen, and L. Cohen, “Optimizing Polyphase-Coded FM Waveforms within a LINC Transmit Architecture,” *2014 IEEE Radar Conference*, Cincinnati, Ohio, May 2014, pp. 835-839.

[15] S.D. Blunt, J. Jakabosky, M. Cook, J. Stiles, S. Sequin, and E.L. Mokole, “Polyphase-Coded FM (PCFM) Radar Waveforms, Part II: Optimization,” *IEEE Transactions on Aerospace and Electronic Systems*, Vol. 50, No. 3, July 2014, pp. 2230-2241.

[16] J. Jakabosky, L. Ryan, and S. Blunt, “Transmitter-in-the-Loop Optimization of Distorted OFDM Radar Emissions,” *2013 IEEE Radar Conference*, Ottawa, Ontario, Canada, April – May 2013.

[17] D. Eustice, C. Latham, C. Baylis, R. J. Marks and L. Cohen, "Amplifier-in-the-Loop Adaptive Radar Waveform Synthesis," in *IEEE Transactions on Aerospace and Electronic Systems*, vol. 53, no. 2, pp. 826-836, April 2017.

[18] C. Latham, M. Fellows, C. Baylis, L. Cohen and R. J. Marks, "Radar Waveform Optimization for Ambiguity Function Properties and Dynamic Spectral Mask Requirements based on Communication Receiver Locations," *2017 IEEE Radio and Wireless Symposium (RWS)*, Phoenix, AZ, 2017, pp. 147-149.

[19] “Efficiency of Microwave Devices,” *Microwave 101*, https://www.microwaves101.com/ encyclopedias/efficiency-of-microwave-devices

[20] J. de Graaf, H. Faust, J. Alatishe, and S. Talapatra, “Generation of Spectrally Confined Transmitted Radar Waveforms,” *Proceedings of the IEEE Conference on Radar*, 2006, pp. 76-83

[21] J. Martin, *Adaptive Load Impedance Optimization for Power Amplifiers in Reconfigurable Radar Transmitters*, Master’s Thesis, Baylor University, 2012.

[22] D. Wilde, Optimum Seeking Methods, Prentice-Hall, 1964.

[23] Fellows, M.; Baylis, C.; Martin, J.; Cohen, L.; Marks, R.J., “Direct Algorithm for the Pareto Load-Pull Optimization of Power-Added Efficiency and Adjacent-Channel Power Ratio,” *IET Radar, Sonar, and Navigation,* vol. 8, no. 9, pp. 1280-1287, 2014.

[24] Y. Collette and P. Siarry, *Multiobjective Optimization: Principles and Case Studies*, Springer, 2004.

[25] H.C. Calpine and A. Golding, "Some Properties of Pareto-Optimal Choices in Decision Problems," Omega 4, No. 2 (1976): 141-147.

[26] T. Getachew, M. Kostreva, and L. Lancaster. "A Generalization of Dynamic Programming for Pareto Optimization in Dynamic Networks." RAIRO-Operations Research 34.1 (2000): 27-47.

[27] R.T. Marler and J.S. Arora. "Survey of Multi-Objective Optimization Methods for Engineering." Structural and Multidisciplinary Optimization 26.6 (2004): 369-395.

[28] K. Deb, "Multi-Objective Optimization." Search Methodologies, Springer U.S., 2005. 273-316.

[29] I. Das and J. E. Dennis, "Normal-Boundary Intersection: A New Method for Generating the Pareto Surface in Nonlinear Multicriteria Optimization Problems," SIAM J. on Optimization, 631-657, March 1998.

[30] I.Y.Kim and O. de Weck, "Adaptive Weighted Sum Method for Multiobjective Optimization: A New Method for Pareto Front Generation", Structural and Multidisciplinary Optimization, Vol. 31, pp. 105-116, 2006.

[31] J. Sevic, K. Burger, and M. Steer, "A Novel Envelope-Termination Load-Pull Method for ACPR Optimization of RF/Microwave Power Amplifiers," 1998 IEEE MTT-S International Microwave Symposium Digest, June 1998, Vol. 2, pp. 723-726.

[32] F. Raab, P. Asbeck, S. Cripps, P. Kenington, Z. Popovic, N. Pothecary, J. Sevic, and N. Sokal, "RF and Microwave Power Amplifier and Transmitter Topologies, Part 1," *High Frequency Electronics*, May 2003.

[33] E. Arroyo-Huerta, A. Diaz-Mendez, J. Ramirez Cortes, and J. Garcia, "An Adaptive Impedance Matching Approach Based on Fuzzy Control," *52nd IEEE International Midwest Symposium on Circuits and Systems*, August 2009, pp. 889-892.

[34] J. Hemminger, "Antenna Impedance Matching With Neural Networks," *International Journal of Nerual Systems* (IJNS), Vol. 15, No. 5, pp. 357-361, 2005.

[35] A. Mushi, D. Johns, and A. Sedra, "Adaptive Impedance Matching," Proceedings of the IEEE International Symposium on Circuits and Systems, 1994 (ISCAS '94), Vol. 2, pp. 69-72.

[36] J. Barkate, A. Tsatsoulas, C. Baylis, L. Cohen and R. J. Marks, "Comparison of Multidimensional Circuit Optimization Techniques for Real-Time Transmitter Use," *2016 Texas Symposium on Wireless and Microwave Circuits and Systems*, Waco, Texas, April 2016.

[37] M. Fellows, L. Lamers, C. Baylis, L. Cohen and R. J. Marks, "A Fast Load-Pull Optimization for Power-Added Efficiency under Output Power and ACPR Constraints," *IEEE Transactions on Aerospace and Electronic Systems*, Vol. 52, No. 6, December 2016, pp. 2906-2916.

[38] C. Baylis, M. Fellows, J. Barkate, A. Tsatsoulas, S. Rezayat, L. Lamers, R.J. Marks II, and L. Cohen, "Circuit Optimization Algorithms for Real-Time Spectrum Sharing Between Radar and Communications," *2016 IEEE Radar Conference* (RadarConf), Philadelphia, PA, May 2016.

[39] M. Fellows, M. Flachsbart, J. Barlow, C. Baylis and R. J. Marks, "The Smith tube: Selection of radar chirp waveform bandwidth and power amplifier load impedance using multiple-bandwidth load-pull measurements," *WAMICON 2014*, Tampa, FL, 2014, pp. 1-5.

[40] J. Barkate, M. Flachsbart, Z. Hays, M. Fellows, J. Barlow, C.Baylis, L. Cohen, and R.J. Marks II, "Fast, Simultaneous Optimization of Power Amplifier Input Power and Load Impedance for Power-Added Efficiency and Adjacent-Channel Power Ratio using the Power Smith Tube," *IEEE Transactions on Aerospace and Electronic Systems*, Vol. 52, No. 2, April 2016, pp. 928-937.

[41] M. Fellows, S. Rezayat, J. Barlow, J. Barkate, A. Tsatsolous, C. Baylis, L. Cohen, R. Marks II, "The bias smith tube: Simultaneous optimization of bias voltage and load impedance in power amplifier design," *2016 IEEE Radio and Wireless Symposium (RWS)*, Austin, TX, 2016, pp. 215-218.

[42] D. Qiao, R. Molfino, S. M. Lardizabal, “An Intelligently Controlled RF Power Amplifier With a Reconfigurable MEMS-Varactor Tuner,” *IEEE Transactions on Microwave Theory and Techniques*, Vol. 53, No. 3, Part 2, March 2005, pp. 1089-1095.

[43] Y. Sun, J. Moritz and X. Zhu, "Adaptive impedance matching and antenna tuning for green software-defined and cognitive radio," *2011 IEEE 54th International Midwest Symposium on Circuits and Systems (MWSCAS)*, Seoul, 2011, pp. 1-4.

[44] Jeffrey Frank Jones, *24 Volumes Combined: NEETS - U.S. Navy Electricity and Electronics Training Series*,1999, pp. 3-17.

[45] J.-S. Fu and A. Mortazawi, “Improving Power Amplifier Efficiency and Linearity Using a Dynamically Controlled Tunable Matching Network,” *IEEE Transactions on Microwave Theory and Techniques*, Vol. 56, No. 12, December 2008, pp. 3239-3244.

[46] A. Semnani, M. Abu Khater, Y.-C. Wu, and D. Peroulis, “An Electronically-Tunable High-Power Impedance Tuner with Integrated Closed-Loop Control,” *IEEE Microwave and Wireless Components Letters*, Vol. 27, No. 8, August 2017, pp.754-756.

[47] Z. Hays, C. Kappelmann, S. Rezayat, M. Fellows, L. Lamers, M. Flachsbart, J. Barlow, C. Baylis, E. Viveiros, A. Darwish, A. Hedden, J. Penn, and R.J. Marks II, "Real-Time Amplifier Optimization Algorithm for Adaptive Radio using a Tunable-Varactor Matching Network," *2017 IEEE Radio and Wireless Symposium (RWS)*, Phoenix, Arizona, January 2017, pp. 215 217.

[48] M. Abu Khater, Y. C. Wu and D. Peroulis, "Tunable Cavity-Based Diplexer With Spectrum-Aware Automatic Tuning," *IEEE Transactions on Microwave Theory and Techniques*, Vol.65, No. 3, pp. 934-944, March 2017.

[49] X. Liu, L. P. B. Katehi, W. J. Chappell and D. Peroulis, "High-Q Tunable Microwave Cavity Resonators and Filters Using SOI-Based RF MEMS Tuners," *Journal of Microelectromechanical Systems*, vol. 19, no. 4, Aug. 2010, pp. 774-784.

[50] M. Abu Khater and D. Peroulis, "Real-Time Feedback Control System for Tuning Evanescent-Mode Cavity Filters," *IEEE Transactions on Microwave Theory and Techniques*, Vol. 64, No. 9, September 2016, pp. 2804-2813.

[51] A. Semnani and D. Peroulis, “Nano-Plasma Tunable Evanescent-Mode Cavity Resonators,” *2014 IEEE MTT-S International Microwave Symposium (IMS)*, Tampa, Florida, June 2014.

[52] J.H. Spears, W.E. Smith, C. Sui, and Y. Zhu, “Methods for Tuning an Adaptive Impedance Matching Network with A Look-Up Table,” U.S. Patent 8,421,548, 2013.

[53] N. Deve, A. B. Kouki and V. Nerguizian, "A compact size reconfigurable 1-3 GHz impedance tuner suitable for RF MEMS applications," *Proceedings. The 16th International Conference on Microelectronics, 2004. ICM 2004.*, 2004, pp. 101-104.

[54] H.M. Nemati, C. Fager, U. Gustavsson, R. Jos, and H. Zirath, “Design of Varactor-Based Tunable matching Networks for Dynamic Load Modulation of High Power Amplifiers,” *IEEE Transactions on Microwave Theory and Techniques*, Vol. 57, No. 5, May 2009, pp. 1110-1118.

[55] Q. Shen and N.S. Barker, "Distributed MEMS Tunable Matching Network Using Minimal-Contact RF-MEMS Varactors," *IEEE Transactions on Microwave Theory and Techniques*, Vol. 54, No. 6, June 2006, pp. 2646-2658.

[56] C. Hoarau, N. Corrao, J.-D. Arnold, P. Ferrari, and P. Xavier, "Complete Design and Measurement Methodology for a Tunable RF Impedance Matching Network," *IEEE Transactions on Microwave Theory and Techniques*, Vol. 56, No. 11, October 2008, pp. 2620-2627.

[57] R.G. Meyer and M.L. Stephens, "Distortion in Variable-Capacitance Diodes," *IEEE Journal of Solid-State Circuits*, Vol. 10, No. 2, February 1975, pp. 47-54.

[58] K. Buisman, L.C.N. de Breede, L.E. Larson, M. Spirito, A. Akhnoukh, T.L.M. Scholtes, and L.K. Nanver, "Distortion Free Varactor Diode Technologies for RF Adaptivity," *2005 IEEE MTT-S International Microwave Symposium*, Long Beach, California, June 2005, pp. 157-160.

[59] S.-J. Park and G.M. Rebeiz, "Low-Loss Two-Pole Tunable Filters With Three Different Predefined Bandwidth Characteristics," *IEEE Transactions on Microwave Theory and Techniques*, Vol. 56, No. 5, May 2008, pp. 1137-1148.